

Topological magnon insulators in two-dimensional van der Waals ferromagnets CrSiTe₃ and CrGeTe₃: towards intrinsic gap-tunability

Fengfeng Zhu,^{1,2,*} Lichuan Zhang,^{3,4,†} Xiao Wang,^{1,†} Flaviano José dos Santos,^{3,5} Junda Song,¹ Thomas Mueller,¹ Karin Schmalzl,⁶ Wolfgang F. Schmidt,⁶ Alexandre Ivanov,⁷ Jitae T. Park,⁸ Jianhui Xu,^{9,8} Jie Ma,² Samir Lounis,^{3,10} Stefan Blügel,³ Yuriy Mokrousov,^{3,11,‡} Yixi Su,^{1,§} and Thomas Brückel¹²

¹*Jülich Centre for Neutron Science (JCNS) at Heinz Maier-Leibnitz Zentrum (MLZ),
Forschungszentrum Jülich, Lichtenbergstrasse 1, D-85747 Garching, Germany*

²*Department of Physics and Astronomy, Shanghai Jiao Tong University, 200240 Shanghai, China*

³*Peter Grünberg Institut and Institute for Advanced Simulation,
Forschungszentrum Jülich and JARA, 52425 Jülich, Germany*

⁴*Department of Physics, RWTH Aachen University, 52056 Aachen, Germany*

⁵*Theory and Simulation of Materials (THEOS), and National Centre for
Computational Design and Discovery of Novel Materials (MARVEL),
École Polytechnique Fédérale de Lausanne, 1015 Lausanne, Switzerland*

⁶*Jülich Centre for Neutron Science (JCNS) at ILL,
Forschungszentrum Jülich, F-38000 Grenoble, France*

⁷*Institut Laue-Langevin, 71 Avenue des Martyrs CS 20156, 38042 Grenoble Cedex 9, France*

⁸*Heinz Maier-Leibnitz Zentrum (MLZ), Technische Universität München, D-85747 Garching, Germany*

⁹*Helmholtz-Zentrum Berlin für Materialien und Energie GmbH,
Hahn-Meitner-Platz 1, D-14109 Berlin, Germany*

¹⁰*Faculty of Physics, University of Duisburg-Essen and CENIDE, 47053 Duisburg, Germany*

¹¹*Institute of Physics, Johannes Gutenberg University Mainz, 55099 Mainz, Germany*

¹²*Jülich Centre for Neutron Science JCNS and Peter Grünberg Institut PGI,
JARA-FIT, Forschungszentrum Jülich, D-52425 Jülich, Germany*

The bosonic analogues of topological insulators have been proposed in numerous theoretical works, but their experimental realization is still very rare, especially for spin systems. Recently, two-dimensional (2D) honeycomb van der Waals (vdW) ferromagnets have emerged as a new platform for topological spin excitations. Here, via a comprehensive inelastic neutron scattering study and theoretical analysis of the spin-wave excitations, we report the realization of topological magnon insulators in CrXTe₃ (X=Si, Ge) compounds. The nontrivial nature and intrinsic tunability of the gap opening at the magnon band-crossing Dirac points are confirmed, while the emergence of the corresponding in-gap topological edge states is demonstrated theoretically. The realization of topological magnon insulators with intrinsic gap-tunability in this class of remarkable 2D materials will undoubtedly lead to new and fascinating technological applications in the domain of magnonics and topological spintronics.

I. INTRODUCTION

Recent theoretical predictions and experimental realizations of exotic quasi-particles and topological excitations in condensed matter have led to a tremendous research interest in topological quantum materials [1–5]. The topology of the electronic band structure is closely linked to the Berry curvature in the k -space [6, 7], for which the spin-orbit coupling (SOC) plays a key role. In principle, it is also possible to realize non-trivial topology in a bosonic system, such as a system of magnonic excitations [8–18], since the band topology can be treated independently from the statistical nature of the particles. Such topological excitations and the corresponding non-trivial in-gap edge states are chiral and robust against disorder, it is thus believed that the emergence and manipulation of the topological magnonic states bares a tremendous promise for future applications in magnonics and topological spintronics, such as e.g. quantized pumping of magnons [19], spin-wave beam splitter [10], magnon waveguides [20], chiral travelling-wave magnon amplifiers [21] and magnon-driven orbitronics [22].

However, in contrast to the case of fermionic systems, the topological excitations have been realized only in very few bosonic systems. This is largely owing to the lack of suitable candidate materials as well as to the tremendous

* These authors contributed equally to this work.; Corresponding author. E-mail: f.zhu@fz-juelich.de

† These authors contributed equally to this work.

‡ Corresponding author. E-mail: y.mokrousov@fz-juelich.de

§ Corresponding author. E-mail: y.su@fz-juelich.de

challenges in experimental probes of uncharged bosonic topological excitations, and, in particular, in a direct detection of in-gap surface/edge states. For instance, inelastic neutron scattering may be the method of choice e.g. for disentangling topological excitation gaps, but, to directly probe the in-gap edge excitation mode is unfortunately beyond its reach even with the most powerful neutron instruments available nowadays. Nevertheless, since topological magnon edge states contribute to the transverse thermal Hall conductivity, it has recently been demonstrated that the nontrivial topological nature of the magnonic bands can be manifested experimentally by the thermal Hall effect even in a charge-neutral spin system [23–26]. Following the pioneering study of the magnon thermal Hall effect in the pyrochlore ferromagnet $\text{Lu}_2\text{V}_2\text{O}_7$ [23, 24], the evidence for the gapped magnonic topological insulating phase was reported in the Ising-like kagome ferromagnet $\text{Cu}[1,3\text{-bdc}]$ under applied magnetic field via inelastic neutron scattering [8]. The search for topological excitations in various spin systems has been intensified since then. Recently, Dirac magnons that exhibit symmetry-protected band crossings have been observed in a three-dimensional (3D) Heisenberg antiferromagnet Cu_3TeO_6 [15, 16] and in a 3D quantum XY magnet CoTiO_3 [17]. Meanwhile, 2D honeycomb vdW magnets [27–29], such as the 2D ferromagnets CrGeTe_3 and Fe_3GeTe_2 as well as the Kitaev material $\alpha\text{-RuCl}_3$, have attracted tremendous research interest owing to their fascinating physical properties. Since the recent observation of the gapped topological excitations in ferromagnetic CrI_3 [11], 2D vdW honeycomb-lattice magnets start to emerge as a unique platform for the exploration of the topological magnonics [9, 12, 14]. In this class of materials, as schematically shown in Fig.1(a), a topological gap can be opened at the magnon band-crossing Dirac points when a sufficiently large SOC is present. Pronounced SOC would in turn give rise to antisymmetric or anisotropic exchange interactions – such as the Dzyaloshinskii-Moriya (DM) [30] and Kitaev interactions – which can drive non-trivial magnonic topology.

While the current research focus of the community falls primarily on few-layer vdW heterostructures and Morié superlattices, a variety of recently discovered quantum phenomena in bulk vdW materials – e.g. the half-integer thermal quantum Hall effect and fractionalized Majorana fermions in $\alpha\text{-RuCl}_3$ [29] or topological magnetic textures in Fe_3GeTe_2 [28] – clearly indicate the potential of bulk 2D vdW magnetic materials as a rich playground in topological quantum matter research. A thorough understanding of intrinsic magnetic interactions and emergent topological properties in single-crystal bulk samples will undoubtedly stimulate further research on monolayer, few-layer and Morié-based counterparts. In this context, 2D vdW CrXTe_3 compounds emerge as one of the very promising representatives in this class. In fact, one would expect the existence of topological magnons in CrXTe_3 similarly to CrI_3 [9, 18, 26], as long as SOC and the antisymmetric exchange interactions are strong enough in this ferromagnetic honeycomb system. Furthermore, due to high versatility in terms of chemical composition, a range of topological magnon insulators with intrinsic gap-tunability may be realized in CrXTe_3 family. As such, the intrinsic control of topological magnon properties, for instance, via the engineering of DM interaction, may lead to novel applications in magnonic spintronics and quantum technology.

In this work, we present a comprehensive inelastic neutron scattering study of the spin-wave excitations in single-crystal CrSiTe_3 and CrGeTe_3 , which belong to a family of 2D vdW honeycomb ferromagnets. Our inelastic neutron scattering experiments performed at low temperatures show clear dispersive magnonic bands and a well-resolved band gap opening at the high-symmetry K points in the Brillouin zone (BZ). By fitting to experimental data within the linear spin-wave theory (LSWT), the magnitude of exchange interactions in studied materials has been determined. Moreover, the observed band gap opening was ascribed to the antisymmetric exchange interactions, namely the DM interaction, and a spin Hamiltonian model including the second-nearest-neighbor (2nd-NN) DM interaction could provide a very good description of the magnonic dispersion in CrXTe_3 . In line with expectations, the size of the topological gap was found to be strongly dependent on the strength of the DM interaction that intrinsically originates from SOC in this system. Furthermore, the Chern numbers of the magnonic bands were found to be non-zero, thus indicating that the band gap opening is indeed topologically nontrivial and corresponding edge states could emerge inside the gap. By assessing theoretically the magnitude of the thermal Hall effect we find that the topologically nontrivial features could be detected in thermal transport measurements in two considered systems. Based on the compelling evidence obtained in our inelastic neutron scattering experiments and theoretical calculations, we thus conclude that the exotic topological magnon insulator, that is intrinsically gap-tunable, can be ideally realized in the family of 2D vdW honeycomb ferromagnets CrXTe_3 .

II. RESULTS AND DISCUSSION

High-quality single crystals of CrXTe_3 ($X=\text{Si, Ge}$) were grown by the flux method, and were carefully examined by X-ray Laue, single-crystal X-ray and neutron diffraction. The Cr^{3+} ions with $S = 3/2$ in CrXTe_3 ($X=\text{Si, Ge}$) occupy an ABC stacked honeycomb lattice, as shown in Fig.1(b). Despite the presence of the Si/Ge atoms, each layer shares a similar atomic structure to that of the chromium trihalides CrI_3 [31] and CrBr_3 at low temperature. All the Cr^{3+} ions are located in the center of the edge-shared trigonal distorted octahedra (D_{3d} symmetry) composed of Te atoms, as shown in Fig.1(c). Below T_c , both materials exhibit ferromagnetic order with the magnetic moments aligned along

the c axis. As shown in Fig.S1, the magnetic susceptibilities measured with fields applied along the a and c axes clearly show ferromagnetic phase transitions occurring at ~ 33 K and ~ 63 K for CrSiTe_3 and CrGeTe_3 respectively, with the easy axis along the c axis. As the isothermal magnetization curves shown in Fig.S1, their magnetic moments can be easily aligned and saturated along both the a and c axes by an application of a small magnetic field, which indicates a small magnetic anisotropy energy in these two materials, consistent with the previous magnetization measurements [32–35]. In addition, the ferromagnetic transitions are further confirmed by neutron diffraction and the transition temperatures T_c are extracted from the fitting of the temperature dependent intensity of the (1,1,0) magnetic Bragg peak. Among them, the magnetic moment direction of CrGeTe_3 in the ferromagnetic phase is determined along the c axis by polarized neutron diffraction, as shown in Fig.S2.

In Fig.2, we show the magnon spectra of CrSiTe_3 along the high-symmetry directions $[-1, H, 0]$ and $[H, H, 3]$ in the $(H, K, 0)$ reciprocal plane as well as along the $[1, 1, L]$ direction in the (H, H, L) reciprocal plane. The measured momentum transfer Q positions in reciprocal space are shown as the black solid lines in the inset of Fig.2(c). The measured magnon bands lie below 16 meV and show clear dispersion along all directions. As shown in Fig.2(a), the low-energy magnon mode (referred to as “acoustic” magnon mode) emerges from the BZ center Γ point and reaches its maximum energy with a gap opening at the M point of the in-plane BZ boundary, consistently with its ferromagnetic nature. Along the $[H, H, 3]$ direction, in the vicinity of the K points, as shown in the Fig.2(b), a small spin gap is faintly visible at $E \approx 9$ meV. Besides, as highlighted by the white arrow in the inset of Fig.2(b), a new branch connected to the acoustic magnon mode was observed along the BZ boundary K - M - K' direction although its intensity is rather weak. From a zoom-in plot in Fig.2(g), the high-energy branch (referred to as “optical” magnon mode) is found to be less dispersive as compared to the acoustic magnon mode, and it also seems disconnected from the acoustic branch at K points. To further confirm whether a magnon gap is opened at the K point, the line profiles of the constant- Q scans at two different K points are shown in Fig.2(h), where a gap opening of about 2 meV can be clearly resolved. Subsequently, the maximum of the acoustic and the minimum of the optical magnon mode at the K point are determined as 8.6(1) meV and 10.7(1) meV by the multi-peak fitting, respectively. Given that the magnitude of the gap is quite large and no clear phonon modes are observed, we conclude that the magnon-phonon hybridization is unlikely to be the origin of the observed gap opening. Instead, introducing an antisymmetric exchange interaction, such as the DM interaction, into the spin Hamiltonian could potentially induce such a considerable gap at the K point. As for the $[1, 1, L]$ direction, the acoustic magnon mode only extends up to 2 meV, which is much smaller than that in the Γ - M and Γ - K directions, indicating that the coupling between vdW layers is notably weak and that the magnon spectra are mainly dictated by the intra-layer exchange interactions.

As for the analogous CrGeTe_3 , whose transition temperature T_c is nearly doubled as compared to that of CrSiTe_3 , we also measured its spin waves along all high-symmetry directions, and the black solid lines in the inset of Fig.3(b) show the corresponding Q positions for the measurements. The magnon modes in the $(H, K, 0)$ reciprocal plane are shown in Fig.3(a), where two branches, namely the acoustic and optical modes, can be easily distinguished, and the magnon modes along $[1, 1, L]$ directions, dictated by the inter-layer exchange interactions, are shown in Fig.3(b). As expected, the acoustic mode has a stronger dispersion than the optical mode and also emerges from the magnetic BZ center Γ point at low energy. Except for the scale of the energy transfers, the overall feature of the magnon modes of CrGeTe_3 appears very similar to that of CrSiTe_3 including the gap opening at the K point. Interestingly, the acoustic magnon mode in the $(H, K, 0)$ plane reaches its energy maximum at around 15 meV which is nearly two times that of CrSiTe_3 , but along the out-of-plane direction, the magnon mode only extends to 2.5 meV, basically the same as in CrSiTe_3 . It indicates that replacing the Si atoms by heavier Ge atoms in CrXTe_3 will significantly enhance the intra-layer exchange interactions and meanwhile will have little influence on the interlayer exchange interactions. This suggests that the exchange interactions can be tuned by nonmagnetic atoms without destroying the magnetic network, and that the strength of SOC of non-magnetic atoms may also play an important role in the super-exchange interactions in this vdW honeycomb ferromagnet family.

Furthermore, one can notice that the optical mode of CrGeTe_3 is rather broad in energy even after taking into consideration the instrument resolution of ~ 2 meV at such energy transfer, and is quite intense, in contrast to the situation of CrSiTe_3 . In fact, we find that the intensity of this optical magnon branch at the K point is about 4 times higher than the prediction of our LSWT calculation. Given that the optical phonon mode of CrGeTe_3 has a similar energy scale [36], and that the evidence for the spin-lattice coupling in CrGeTe_3 has been already reported in previous Raman experiments [37, 38], we tend to believe that both the broadening in energy and the intensity enhancement could be a result of possible magnon-phonon interactions. Interestingly, the phonon modes around 25 meV are indeed mainly contributed by the magnetic atoms Cr [39], the coexistence of the phonon and magnon modes in the same energy range may allow for a possible spectral weight transfer between them, thus leading to the observed unusual intensity enhancement. Generally, a dynamic spin-lattice coupling can create hybridization gaps or broadening in the magnon spectra at the intersection points of the coupled magnon and phonon modes.

Regardless of the unusual broadening of the optical branches, a gap opening at the K point is still resolvable. In Fig.3(e)-(g), three line profiles of energy scans are extracted from the vicinity of the K point and fitted by two Gauss

peaks to accurately determine the size of the opened gap, and the corresponding positions of momentum transfer in reciprocal space in the measurements are marked by the black circles in Fig.(h)-(j). From Fig3.(f), a weak but clear shoulder can be seen around 15 meV which denotes the band maximum of the acoustic mode, and subsequently the size of the opened gap at the K point can be determined as ~ 5 meV from the fitting results. We conclude that such a large gap is unlikely to arise as a result of possible magnon-phonon coupling, since the magnon-phonon coupling induced gap always occurs at the intersection between the magnon and phonon bands and it does not extend over the entire BZ. It is thus expected that the gap in CrGeTe₃ shares the same origin as in CrSiTe₃, namely the antisymmetric exchange interaction e.g. like the SOC-mediated DM interaction. Hence, it appears natural that a larger gap opening in CrGeTe₃ must arise from the larger SOC in the latter material when Si is replaced by heavier Ge.

In order to determine the nature of magnon bands and the underlying magnetic exchange interactions in CrXTe₃ systems, we carry out LSWT calculations based on a generalized Heisenberg spin Hamiltonian including DM interaction and single-ion magnetic anisotropy [40]:

$$H = - \sum_{i < j} J_{ij} (\mathbf{S}_i \cdot \mathbf{S}_j) - A_{zz} \sum_i (S_i^z)^2 - \sum_{i < j} \mathbf{D}_{ij} \cdot (\mathbf{S}_i \times \mathbf{S}_j), \quad (1)$$

where J_{ij} is the Heisenberg exchange constant between spins \mathbf{S}_i and \mathbf{S}_j , \mathbf{D}_{ij} represents the vector of the DM interaction between two magnetic ions when the inversion symmetry is broken, and A_{zz} is the easy-axis anisotropy along the c axis. Note that we take $S = 3/2$ given that the measured moment of Cr ions is extracted as $\sim 3 \mu_B$ from the isotherm magnetization curve shown in Fig.S1. As illustrated in Fig.1(b), we consider the 1st- and 2nd-NN Heisenberg exchange couplings in every honeycomb plane labeled as J_{ab1} and J_{ab2} , and the 1st- and 2nd-NN exchange couplings between layers labeled as J_{c1} and J_{c2} . From the symmetry analysis, there will be no DM interaction between the nearest neighbors (NN), because of the space inversion. However, the space inversion symmetry is broken between the 2nd NN, which can lead to a non-zero 2nd-NN DM interaction.

After a proper fitting process of the experimentally observed magnon spectra along the high-symmetry directions, the best-fit values for the exchange parameters of CrSiTe₃ and CrGeTe₃ were extracted. As shown in Table.1, we find that the intra-layer interactions in CrXTe₃ are mainly dominated by the NN exchange couplings J_{ab1} which are one order of magnitude larger than the interlayer exchange. Given the presence of sizeable interlayer exchange interactions, it is worth noting that CrXTe₃, strictly speaking, should be classified as quasi-2D spin systems. While the direct exchange coupling between Cr ions is expected to be anti-ferromagnetic, due to the formation of Cr-Te-Cr bonds with a bond angle of nearly 90 degrees, the NN exchange couplings among Cr ions become ferromagnetic ($J > 0$) according to the Goodenough-Kanamori-Anderson rules [41]. Interestingly, although the fitting values of the inter-layer couplings J_{c1} and J_{c2} are quite comparable, the magnon dispersion along [00L] direction is likely much more sensitive to the 2nd-NN inter-layer coupling J_{c2} because each Cr³⁺ spin has nine 2nd-NNs but only one 1st NN. Besides, the strength of the DM interactions is fitted as $|\mathbf{D}_{ij}| = 0.12$ meV for CrSiTe₃ and $|\mathbf{D}_{ij}| = 0.32$ meV for CrGeTe₃ which results in a ~ 2 meV and ~ 5 meV gap opening at the K points, respectively. We remark that the magnitude of the DM interaction in CrXTe₃ constitutes about 10% of J_{ab1} and it is quite comparable to the value of exchange J_{ab2} between 2nd-NN Cr ions. From the isothermal magnetization curve at 2 K (Fig.S1), we can extract the magneto-crystalline anisotropy energy per Cr³⁺, which is only 0.09 meV for CrSiTe₃ and 0.02 meV for CrGeTe₃, indicating a small single-ion anisotropy in the CrXTe₃ system. In terms of the small single-ion anisotropy, as expected, we failed to determine the size of the gap at the Γ point from our energy-scan data directly, and we used instead the quadratic fitting result 0.01 meV (shown in Fig.S5 and Fig.S6) for the anisotropy term A in the Heisenberg-DM model.

As shown in Figs.2(d)-(f) and Figs.3(c)(d), the magnon bands of CrXTe₃ calculated from the Heisenberg-DM model are consistent with our experimentally observed spectra, taking into account a finite energy resolution. Especially in the vicinity of the K points, the opened gap is also well described by the model. In addition, a range of constant-energy slices near the BZ boundary are found to be in an excellent agreement with the simulation results, as shown in Fig.S4. Moreover, the calculated spectra also reproduce the characteristic weak/strong-intensity of the magnon bands in different BZs, except that the optical modes of CrGeTe₃ are significantly enhanced by the possible hybridization with the phonon modes, as discussed above.

The overall band dispersion is mainly determined by the ferromagnetic NN Heisenberg exchange couplings, and the gap opening at the K points cannot be reproduced by simply adding exchange couplings with further neighbors in the model, until an anisotropic exchange coupling term such as the DM interaction is taken into consideration. It is known that the DM interaction acts as an effective gauge potential for magnonic states and it can open topologically nontrivial band gaps in a magnonic system [9, 42]. Without the DM interaction, a crossing point located in the vicinity

of K point would be present, Fig.4(a), while the gap is opened immediately as the DM interaction is introduced, with the band gap size increasing almost linearly with the strength of the DM interaction, Fig.4(b). Overall, the constructed Heisenberg-DM model reproduces spin waves in CrXTe_3 very nicely, with one key point being that the DM interaction in our case is not only dependent on the SOC strength of Te atoms along the Cr-Te-Cr paths, but it is also influenced by Si/Ge atoms. The large difference of the gap size in CrXTe_3 thus translates into a possibility to tune the DM interaction by the substitution of the atoms with different SOC strength in the honeycomb center.

Interestingly, in addition to the Heisenberg-DM model, introducing the Kitaev interactions can also produce similar spin wave spectra and induce a gap opening at the K points. If we exclude X atoms, the rest of CrXTe_3 shares a common atomic structure with the well-studied Kitaev spin liquid candidate $\alpha\text{-RuCl}_3$ [43], and three kinds of diamond-shaped planes, composed of the nearest-neighbor Cr-Te-Cr bonds, are nearly orthogonal to each other. In terms of the structure symmetry, it is possible to have an anisotropic exchange interaction between nearest neighbors, for instance, an anisotropic Ising interaction in the local basis that consists of the normal vectors of three Cr-Te-Cr planes, as shown in Fig.S7. The presence of the additional anisotropy can make it possible to construct the Heisenberg-Kitaev Hamiltonian. Surprisingly, in order to match the magnetic excitations in CrXTe_3 , we found that the Kitaev exchange needs to be one order of magnitude larger than the NN Heisenberg term, as shown in Table.S1. In the latter case, the fitted Kitaev exchange parameters of CrGeTe_3 are almost two times those of CrSiTe_3 , which is quite interesting, since CrSiTe_3 and CrGeTe_3 share a similar local environment including the bond distance for NN Cr atoms. One possible explanation would be that the sp^3 hybridized orbitals of Si/Ge atoms in the honeycomb center are strongly coupled with the p orbitals of Te atoms and subsequently strongly influence the strength of the Cr-Te-Cr super-exchange interaction. Similar orbital hybridization effect is not rare since the super-exchange interaction mediated by nonmagnetic ions is also proposed in inverse-trirutile compound [44] and double-perovskites [45]. In any case, if CrXTe_3 is dominated by the Kitaev interaction, then a strong in-plane anisotropy should be easily evident in the magnetization measurements, which has never been reported. We thus conclude that the Heisenberg-Kitaev model is not a proper model for CrXTe_3 . More details concerning the discussion of Heisenberg-Kitaev model are given in the supplement.

Having determined the microscopic spin Hamiltonians for CrXTe_3 , we turn to the analysis of the topological nature of the magnonic bands, and reveal theoretically the presence of a large thermal Hall effect, an unambiguous experimental signature of topologically nontrivial in-gap edge states. Our numerical calculations confirm a nonzero Berry curvature at the K points and also a nonzero Chern number, indicating nontrivial topology of these magnon bands. For bulk CrXTe_3 , the total Chern number is determined to be -3 and $+3$ for the acoustic and optical magnon bands respectively, which means there is one topological edge state at the boundary of each honeycomb layer. It is important to note that the sign of the Chern number depends on the magnetization direction which in our case is the z -axis. The sign of the Chern number can be changed by reversing the magnetization direction, which can be naturally achieved at the magnetic domain walls in CrXTe_3 acting as perfect waveguides for the topological edge states. In addition to the bulk system, we also investigated the topological properties of the monolayer system, where we observe an almost identical BZ Berry curvature distribution and predict only one acoustic branch with Chern number -1 and one optical branch with Chern number $+1$ for the magnon bands. Due to the lack of any interlayer interactions, the magnon bands in the monolayer are not split as in the bulk, but the topological properties are sustained as long as the intra-layer DM interaction exists. To simplify the calculation, we use the monolayer system to study the edge states. The edge states of zigzag and armchair nanoribbons with the projections of the bulk states are shown together in Fig.4(c) and (d), where one can observe that the edges on the two sides of a nanoribbon hold their own exclusive edge states but with opposite propagation direction. The role of the DM interaction here is similar to that of strong SOC in graphene-like systems which turns them into a quantum spin Hall insulator [2], and so CrXTe_3 can be also considered as a bosonic version of the well-known topological insulator state. Correspondingly, the presence of nontrivial edge states can contribute to the transverse thermal Hall conductivity to yield the topological thermal Hall effect when a longitudinal temperature gradient and out-of-plane magnetic field are applied. As shown in Fig.4(e), our numerical estimates indicate that the thermal Hall conductivity generated by the edge states can reach the order of 10^{-4} W/Km, which is large enough to be observed in experiment. This motivates the future confirmation of topological thermal Hall effect in CrXTe_3 from thermal transport experiments.

In summary, we carried out a very comprehensive inelastic neutron scattering study of the spin-wave excitations on the ferromagnetic honeycomb magnets CrXTe_3 . Our data shows a clear gap opening in the magnon bands at the K points, with the gap size of about 2 meV and 5 meV for CrSiTe_3 and CrGeTe_3 , respectively. The magnon band dispersion in CrXTe_3 can be described very well by either the Heisenberg-DM model or Heisenberg-Kitaev model. The gap opening can be ascribed to the asymmetric DM interaction with an out-of-plane DM vector or Kitaev interactions. However, due to the very small magnetic anisotropy observed in CrXTe_3 , the Heisenberg-DM model, in which the isotropic Heisenberg exchange dominates, is perceived as the proper model for these materials. The magnon spectra of CrXTe_3 are successfully reproduced by using the LSWT calculations. The gap size was found to be proportional to the strength of the DM interaction. The strength of the DM interaction is also strongly dependent on the SOC of the

nonmagnetic Si/Ge atoms that are located at the honeycomb center. Furthermore, our numerical calculations predict the nontrivial topological nature of the magnon bands gap at the K points, and also reveal the existence of topological edge states at the sample boundaries and domain walls. In addition, we also calculated the reference values for the expected thermal Hall conductivity that may arise from the topological magnon edge states, which can be measured in future thermal transport experiments. Based on our experimental and theoretical results, we propose that CrSiTe_3 and CrGeTe_3 present an ideal platform to realize topological magnon insulators, in which the nontrivial magnon gaps can be intrinsically tuned by varying the SOC of nonmagnetic ions. In contrast to CrI_3 , the substitution of Si/Ge in CrXTe_3 system using a wide range of nonmagnetic ions like C, Si, Ge, Sn, Pb, Ga [46–50] can in principle change the balance of the exchange interactions and thus enable the manipulation of the topological magnon gap size, leading to novel magnetic properties rooting in complex magnonic topology.

III. MATERIALS AND METHODS

High-quality single crystals of CrXTe_3 ($\text{X}=\text{Si}, \text{Ge}$) were grown by the flux method at the sample preparation laboratory of JCMS-MLZ in Garching. Starting materials of Cr, X and Te were mixed in an Ar-filled glove box at a molar ratio of $\text{Cr}:\text{X}:\text{Te}=1:1:10$. The mixture was placed in an alumina crucible, which was then sealed in an evacuated quartz tube. The tube was heated up to 930°C ($\text{X}=\text{Ge}$) or 1030°C ($\text{X}=\text{Si}$) in 4 hours and sustained there for 10 hours. Then the tube was slowly cooled down to 600°C with a cooling speed of 3°C/h followed by separating the crystals from the Te flux by centrifuging. Shiny and sizable crystals with hexagonal natural edges were obtained.

Single-crystal X-ray diffraction (XRD) was performed at room temperature with an incident wavelength of 1.54 \AA (Cu-K_α) on a Bruker D2-Phaser X-ray diffractometer. By using a SQUID magnetometer (Quantum Design), the temperature and field dependence of the magnetization of CrSiTe_3 and CrGeTe_3 were measured along both the a and c axes respectively. The magnetic susceptibility was measured from 2 K to 300 K with both zero-field-cooling (ZFC) and field-cooling (FC) conditions for some selected single crystals. The isothermal magnetization ($M-H$) curves were also measured in a sweeping field from -50 to 50 kOe at 2 K.

The polarized neutron diffraction measurement on single-crystal CrGeTe_3 was carried out at the cold-neutron polarized spectrometer DNS at MLZ (with $\lambda_i = 4.2\text{ \AA}$) at $T = 4\text{ K}$. Two-dimensional Q-maps in the $(\text{H}, \text{K}, 0)$ and $(\text{H}, \text{H}, \text{L})$ planes of reciprocal space at three different polarization modes were measured at 4 K. For the measurements of spin-wave excitations, we co-aligned 2 pieces of large single crystals with a total mass of 1.3 g for CrSiTe_3 , and more than 100 pieces with a total mass of about 1.4 g for CrGeTe_3 . All the inelastic neutron scattering experiments were performed by using a range of thermal and cold neutron triple-axis spectrometers, including PUMA at MLZ, FLEXX [51] at HZB, IN12, IN8 and IN22 at ILL. Both the $(\text{H}, \text{H}, \text{L})$ and $(\text{H}, \text{K}, 0)$ oriented samples were prepared for each of CrSiTe_3 and CrGeTe_3 . The low energy magnon dispersion along $[0, 0, \text{L}]$ was measured at the cold neutron triple-axis at IN12 (with a fixed $k_f = 1.7\text{ \AA}^{-1}$ and 2.8 \AA^{-1}) and at FLEXX (with $k_f = 1.55\text{ \AA}^{-1}$). The magnon dispersions along $[\text{H}, \text{H}, 0]$ and $[\text{H}, 0, 0]$ were measured at the thermal neutron triple-axis spectrometers IN8 and PUMA (both with a fixed $k_f = 2.662\text{ \AA}^{-1}$). All the magnon dispersion data was collected at the base temperature of $T = 2\text{ K}$.

IV. SUPPLEMENTARY MATERIALS

Detailed magnetic properties of CrSiTe_3 and CrGeTe_3 .

Detailed analysis of the polarized neutron scattering data for CrGeTe_3 .

Detailed analysis of the inelastic neutron scattering data: constant-energy mapping for CrSiTe_3 , and the determination of the magnon gap at the Brillouin zone center for CrXTe_3 .

Detailed descriptions of the spin Hamiltonian for the Heisenberg-DM model and Heisenberg-Kitaev model.

The calculation of the magnon band topology for CrXTe_3 .

Fig. S1. XRD and magnetic properties of CrSiTe_3 and CrGeTe_3 .

Fig. S2. Polarized neutron scattering on CrGeTe_3 .

Fig. S3. Mosaic width (i.e. FWHM) of the co-aligned CrXTe_3 samples.

Fig. S4. Constant-energy mappings of the magnon spectra of CrSiTe_3 in the $(\text{H}, \text{K}, 0)$ scattering plane measured at the thermal neutron triple-axis spectrometer PUMA.

Fig. S5. The magnon spectra of CrGeTe_3 measured at the cold neutron triple-axis spectrometer IN12.

Fig. S6. Cosine-function curve fittings of the respective magnon band dispersion of CrSiTe_3 and CrGeTe_3 along the $[1, 1, \text{L}]$ direction.

Fig. S7. Schematic plot for the Kitaev model.

Fig. S8. Comparison of the calculated magnon spectra with different models.

Fig. S9. The Berry curvature in the $K_x - K_y$ plane.

Fig. S10. Chern numbers of magnon bands.

Fig. S11. Calculated transverse thermal Hall conductivity.

References[17, 18, 23–27, 32, 34, 35, 40, 43, 47, 48, 52–60]

V. ACKNOWLEDGMENTS

Acknowledgements: We acknowledge Susanne Mayr for assistance with the crystal orientation. This work is based on the experiments performed at DNS, PUMA, IN8, IN12, IN22 and FLEXX neutron instruments. **Funding:** F.Z. acknowledges the funding support from the HGF–OCPC Postdoctoral Program. Y.M. gratefully acknowledges the Jülich Supercomputing Centre and RWTH Aachen University for providing computational resources, as well as the support of Deutsche Forschungsgemeinschaft (DFG, German Research Foundation) – TRR 173 – 268565370 (project A11), TRR 288 – 422213477 (project B06). L.Z gratefully acknowledges the support of China Scholarship Council (CSC) (Grant No. [2016]3100). S. L. acknowledges the funding support provided by the Priority Programme SPP 2244 2D Materials Physics of van der Waals Heterostructures of the Deutsche Forschungsgemeinschaft (DFG) (project LO 1659/7-1) and the European Research Council (ERC) under the European Union’s Horizon 2020 research and innovation programme (ERC-consolidator Grant No. 681405 DYNASORE). S.B. acknowledges financial support by the Deutsche Forschungsgemeinschaft (DFG) within CRC 1238 (project number 277146847, subproject C01). **Author contributions:** F.Z. and Y.S conceived the project. Y.S., Y.M., S.B., T.B. co-supervised the work. X.W. carried out the single-crystal growth. F.Z, X.W., Y.S. carried out the neutron scattering experiments with supports from J.S., T.M., K.S., W.F.S., A.I., J.P., J.X., J.M.. L.Z. carried out the theoretical analysis with supports from F.J.D.S., S.L., Y.M.. F.Z. carried out the X-ray diffraction and magnetization measurements. F.Z., L.Z., Y.S. wrote the manuscript with contributions from all authors. **Competing interests:** The authors declare that they have no competing interests. **Data and materials availability:** All data needed to evaluate the conclusions in the paper are present in the paper and/or the supplementary materials. The raw data taken at the Institut Laue-Langevin (ILL) can be accessed at <https://doi.ill.fr/10.5291/ILL-DATA.4-01-1634> and <https://doi.ill.fr/10.5291/ILL-DATA.CRG-2498>. The raw data taken at the Heinz Maier-Leibnitz Zentrum (MLZ) and at the Berlin Neutron Scattering Center (BENSCH) can be accessed at <https://doi.org/10.5281/zenodo.4963138>.

-
- [1] F. D. M. Haldane, Model for a Quantum Hall Effect without Landau Levels: Condensed-Matter Realization of the “Parity Anomaly”. *Phys. Rev. Lett.* **61**, 2015–2018 (1988).
 - [2] C. L. Kane, E. J. Mele, Z₂ Topological Order and the Quantum Spin Hall Effect. *Phys. Rev. Lett.* **95**, 146802 (2005).
 - [3] M. Z. Hasan, C. L. Kane, Colloquium : Topological insulators. *Rev. Mod. Phys.* **82**, 3045–3067 (2010).
 - [4] X.-L. Qi, S.-C. Zhang, Topological insulators and superconductors. *Rev. Mod. Phys.* **83**, 1057–1110 (2011).
 - [5] N. P. Armitage, E. J. Mele, A. Vishwanath, Weyl and Dirac semimetals in three-dimensional solids. *Rev. Mod. Phys.* **90**, 015001 (2018).
 - [6] N. Nagaosa, J. Sinova, S. Onoda, A. H. MacDonald, N. P. Ong, Anomalous Hall effect. *Rev. Mod. Phys.* **82**, 1539–1592 (2010).
 - [7] D. Xiao, M.-C. Chang, Q. Niu, Berry phase effects on electronic properties. *Rev. Mod. Phys.* **82**, 1959–2007 (2010).
 - [8] R. Chisnell, J. S. Helton, D. E. Freedman, D. K. Singh, R. I. Bewley, D. G. Nocera, Y. S. Lee, Topological Magnon Bands in a Kagome Lattice Ferromagnet. *Phys. Rev. Lett.* **115**, 147201 (2015).
 - [9] S. A. Owerre, A first theoretical realization of honeycomb topological magnon insulator. *J. Phys. Condens. Matter* **28**, 386001 (2016).
 - [10] X. S. Wang, Y. Su, X. R. Wang, Topologically protected unidirectional edge spin waves and beam splitter. *Phys. Rev. B* **95**, 1–5 (2017).
 - [11] L. Chen, J.-H. Chung, B. Gao, T. Chen, M. B. Stone, A. I. Kolesnikov, Q. Huang, P. Dai, Topological spin excitations in honeycomb ferromagnet CrI₃. *Phys. Rev. X* **8**, 041028 (2018).
 - [12] D. G. Joshi, Topological excitations in the ferromagnetic Kitaev-Heisenberg model. *Phys. Rev. B* **98**, 060405 (2018).
 - [13] P. A. Pantaleón, Y. Xian, Edge states in a ferromagnetic honeycomb lattice with armchair boundaries. *Phys. B Condens. Matter* **530**, 191–194 (2018).
 - [14] P. A. McClarty, X.-Y. Dong, M. Gohlke, J. G. Rau, F. Pollmann, R. Moessner, K. Penc, Topological magnons in Kitaev magnets at high fields. *Phys. Rev. B* **98**, 060404(R) (2018).
 - [15] S. Bao, J. Wang, W. Wang, Z. Cai, S. Li, Z. Ma, D. Wang, K. Ran, Z.-Y. Dong, D. L. Abernathy, S.-L. Yu, X. Wan, J.-X. Li, J. Wen, Discovery of coexisting Dirac and triply degenerate magnons in a three-dimensional antiferromagnet. *Nat. Commun.* **9**, 2591 (2018).
 - [16] W. Yao, C. Li, L. Wang, S. Xue, Y. Dan, K. Iida, K. Kamazawa, K. Li, C. Fang, Y. Li, Topological spin excitations in a three-dimensional antiferromagnet. *Nat. Phys.* **14**, 1011–1015 (2018).

- [17] B. Yuan, I. Khait, G.-J. Shu, F. C. Chou, M. B. Stone, J. P. Clancy, A. Paramekanti, Y.-J. Kim, Dirac Magnons in a Honeycomb Lattice Quantum XY Magnet CoTiO_3 . *Phys. Rev. X* **10**, 011062 (2020).
- [18] E. Aguilera, R. Jaeschke-Ubiergo, N. Vidal-Silva, L. E. F. F. Torres, A. S. Nunez, Topological magnonics in the two-dimensional van der Waals magnet CrI_3 . *Phys. Rev. B* **102**, 024409 (2020).
- [19] F. Mei, G. Chen, N. Goldman, L. Xiao, S. Jia, Topological magnon insulator and quantized pumps from strongly-interacting bosons in optical superlattices. *New J. Phys.* **21**, 095002 (2019).
- [20] A. Mook, J. Henk, I. Mertig, Magnon waveguide with nanoscale confinement constructed from topological magnon insulators. *Phys. Rev. B* **91**, 174409 (2015).
- [21] D. Malz, J. Knolle, A. Nunnenkamp, Topological magnon amplification. *Nat. Commun.* **10**, 3937 (2019).
- [22] L.-C. Zhang, D. Go, J.-P. Hanke, P. M. Buhl, S. Grytsiuk, S. Blügel, F. R. Lux, Y. Mokrousov, Imprinting and driving electronic orbital magnetism using magnons. *Commun. Phys.* **3**, 227 (2020).
- [23] H. Katsura, N. Nagaosa, P. A. Lee, Theory of the Thermal Hall Effect in Quantum Magnets. *Phys. Rev. Lett.* **104**, 066403 (2010).
- [24] Y. Onose, T. Ideue, H. Katsura, Y. Shiomi, N. Nagaosa, Y. Tokura, Observation of the Magnon Hall Effect. *Science* **329**, 297–299 (2010).
- [25] R. Matsumoto, S. Murakami, Theoretical Prediction of a Rotating Magnon Wave Packet in Ferromagnets. *Phys. Rev. Lett.* **106**, 197202 (2011).
- [26] S. A. Owerre, Topological honeycomb magnon Hall effect: A calculation of thermal Hall conductivity of magnetic spin excitations. *J. Appl. Phys.* **120**, 043903 (2016).
- [27] C. Gong, L. Li, Z. Li, H. Ji, A. Stern, Y. Xia, T. Cao, W. Bao, C. Wang, Y. Wang, Z. Q. Qiu, R. J. Cava, S. G. Louie, J. Xia, X. Zhang, Discovery of intrinsic ferromagnetism in two-dimensional van der Waals crystals. *Nature* **546**, 265–269 (2017).
- [28] B. Ding, Z. Li, G. Xu, H. Li, Z. Hou, E. Liu, X. Xi, F. Xu, Y. Yao, W. Wang, Observation of Magnetic Skyrmion Bubbles in a van der Waals Ferromagnet Fe_3GeTe_2 . *Nano Lett.* **20**, 868–873 (2020).
- [29] Y. Kasahara, T. Ohnishi, Y. Mizukami, O. Tanaka, S. Ma, K. Sugii, N. Kurita, H. Tanaka, J. Nasu, Y. Motome, T. Shibauchi, Y. Matsuda, Majorana quantization and half-integer thermal quantum Hall effect in a Kitaev spin liquid. *Nature* **559**, 227–231 (2018).
- [30] T. Moriya, New mechanism of anisotropic superexchange interaction. *Phys. Rev. Lett.* **4**, 228–230 (1960).
- [31] M. A. McGuire, H. Dixit, V. R. Cooper, B. C. Sales, Coupling of Crystal Structure and Magnetism in the Layered, Ferromagnetic Insulator CrI_3 . *Chem. Mater.* **27**, 612–620 (2015).
- [32] L. D. Casto, A. J. Clune, M. O. Yokosuk, J. L. Musfeldt, T. J. Williams, H. L. Zhuang, M. W. Lin, K. Xiao, R. G. Hennig, B. C. Sales, J. Q. Yan, D. Mandrus, Strong spin-lattice coupling in CrSiTe_3 . *APL Mater.* **3**, 041515 (2015).
- [33] B. Liu, Y. Zou, L. Zhang, S. Zhou, Z. Wang, W. Wang, Z. Qu, Y. Zhang, Critical behavior of the quasi-two-dimensional semiconducting ferromagnet CrSiTe_3 . *Sci. Rep.* **6**, 33873 (2016).
- [34] D.-H. Kim, K. Kim, K.-T. Ko, J. Seo, J. S. Kim, T.-H. Jang, Y. Kim, J.-Y. Kim, S.-W. Cheong, J.-H. Park, Giant Magnetic Anisotropy Induced by Ligand LS Coupling in Layered Cr Compounds. *Phys. Rev. Lett.* **122**, 207201 (2019).
- [35] J. Zeisner, A. Alfonsov, S. Selzer, S. Aswartham, M. P. Ghimire, M. Richter, J. van den Brink, B. Büchner, V. Kataev, Magnetic anisotropy and spin-polarized two-dimensional electron gas in the van der Waals ferromagnet $\text{Cr}_2\text{Ge}_2\text{Te}_6$. *Phys. Rev. B* **99**, 165109 (2019).
- [36] K. Wang, T. Hu, F. Jia, G. Zhao, Y. Liu, I. V. Solovyev, A. P. Pyatakov, A. K. Zvezdin, W. Ren, Magnetic and electronic properties of $\text{Cr}_2\text{Ge}_2\text{Te}_6$ monolayer by strain and electric-field engineering. *Appl. Phys. Lett.* **114**, 092405 (2019).
- [37] Y. Tian, M. J. Gray, H. Ji, R. J. Cava, K. S. Burch, Magneto-elastic coupling in a potential ferromagnetic 2D atomic crystal. *2D Mater.* **3**, 025035 (2016).
- [38] Y. Sun, R. C. Xiao, G. T. Lin, R. R. Zhang, L. S. Ling, Z. W. Ma, X. Luo, W. J. Lu, Y. P. Sun, Z. G. Sheng, Effects of hydrostatic pressure on spin-lattice coupling in two-dimensional ferromagnetic $\text{Cr}_2\text{Ge}_2\text{Te}_6$. *Appl. Phys. Lett.* **112**, 072409 (2018).
- [39] K. Wang, X. Xu, Y. Cheng, M. Zhang, J. S. Wang, H. Wang, G. Zhang, Magnon relaxation time in ferromagnetic $\text{Cr}_2\text{Ge}_2\text{Te}_6$ monolayer governed by magnon-phonon interaction. *Appl. Phys. Lett.* **118** (2021).
- [40] F. J. dos Santos, M. dos Santos Dias, F. S. M. Guimarães, J. Bouaziz, S. Lounis, Spin-resolved inelastic electron scattering by spin waves in noncollinear magnets. *Phys. Rev. B* **97**, 024431 (2018).
- [41] J. B. Goodenough, *Magnetism and the Chemical Bond* (Interscience-Wiley, New York, 1963).
- [42] S. K. Kim, H. Ochoa, R. Zarzuela, Y. Tserkovnyak, Realization of the Haldane-Kane-Mele Model in a System of Localized Spins. *Phys. Rev. Lett.* **117**, 227201 (2016).
- [43] A. Banerjee, C. A. Bridges, J.-Q. Yan, A. A. Aczel, L. Li, M. B. Stone, G. E. Granroth, M. D. Lumsden, Y. Yiu, J. Knolle, S. Bhattacharjee, D. L. Kovrizhin, R. Moessner, D. A. Tennant, D. G. Mandrus, S. E. Nagler, Proximate Kitaev quantum spin liquid behaviour in a honeycomb magnet. *Nat. Mater.* **15**, 733–740 (2016).
- [44] M. Zhu, D. Do, C. R. Dela Cruz, Z. Dun, H. D. Zhou, S. D. Mahanti, X. Ke, Tuning the Magnetic Exchange via a Control of Orbital Hybridization in $\text{Cr}_2(\text{Te}_{1-x}\text{W}_x)\text{O}_6$. *Phys. Rev. Lett.* **113**, 076406 (2014).
- [45] V. M. Katukuri, P. Babkevich, O. Mustonen, H. C. Walker, B. Fåk, S. Vasala, M. Karppinen, H. M. Rønnow, O. V. Yazyev, Exchange Interactions Mediated by Nonmagnetic Cations in Double Perovskites. *Phys. Rev. Lett.* **124**, 077202 (2020).
- [46] S. Chabungbam, P. Sen, Computational design of a robust two-dimensional antiferromagnetic semiconductor. *Phys. Rev. B* **96**, 045404 (2017).

- [47] H. L. Zhuang, Y. Xie, P. R. C. Kent, P. Ganesh, Computational discovery of ferromagnetic semiconducting single-layer CrSnTe_3 . *Phys. Rev. B* **92**, 035407 (2015).
- [48] I. Khan, J. Hong, High Curie temperature and strain-induced semiconductor-metal transition with spin reorientation transition in 2D CrPbTe_3 monolayer. *Nanotechnology* **31**, 195704 (2020).
- [49] B. Marfoua, J. Hong, Spin Seebeck effect in the 2D ferromagnetic CrPbTe_3 . *Phys. E* **126**, 114443 (2021).
- [50] M. Yu, X. Liu, W. Guo, Novel two-dimensional ferromagnetic semiconductors: Ga-based transition-metal trichalcogenide monolayers. *Phys. Chem. Chem. Phys.* **20**, 6374–6382 (2018).
- [51] M. Le, D. Quintero-Castro, R. Toft-Petersen, F. Groitl, M. Skoulatos, K. Rule, K. Habicht, Gains from the upgrade of the cold neutron triple-axis spectrometer FLEXX at the BER-II reactor. *Nucl. Instruments Methods Phys. Res. Sect. A Accel. Spectrometers, Detect. Assoc. Equip.* **729**, 220–226 (2013).
- [52] J. A. Alonso, D. Serrate, J. M. D. Teresa, M. R. Ibarra, Related content Crystallographic , magnetic and electronic structures of a new layered ferromagnetic Crystallographic , magnetic and electronic structures of a new layered ferromagnetic compound $\text{Cr}_2\text{Ge}_2\text{Te}_6$. *J. Phys. Condens. Matter* **7**, 69 (1995).
- [53] Y. F. Li, W. Wang, W. Guo, C. Y. Gu, H. Y. Sun, L. He, J. Zhou, Z. B. Gu, Y. F. Nie, X. Q. Pan, Electronic structure of ferromagnetic semiconductor CrGeTe_3 by angle-resolved photoemission spectroscopy. *Phys. Rev. B* **98**, 125127 (2018).
- [54] S. Khan, C. W. Zollitsch, D. M. Arroo, H. Cheng, I. Verzhbitskiy, A. Sud, Y. P. Feng, G. Eda, H. Kurebayashi, Spin dynamics study in layered van der Waals single-crystal $\text{Cr}_2\text{Ge}_2\text{Te}_6$. *Phys. Rev. B* **100**, 134437 (2019).
- [55] T. Holstein, H. Primakoff, Field dependence of the intrinsic domain magnetization of a ferromagnet. *Phys. Rev.* **58**, 1098–1113 (1940).
- [56] Y. Singh, S. Manni, J. Reuther, T. Berlijn, R. Thomale, W. Ku, S. Trebst, P. Gegenwart, Relevance of the Heisenberg-Kitaev Model for the Honeycomb Lattice Iridates A_2IrO_3 . *Phys. Rev. Lett.* **108**, 127203 (2012).
- [57] C. Xu, J. Feng, H. Xiang, L. Bellaiche, Interplay between Kitaev interaction and single ion anisotropy in ferromagnetic CrI_3 and CrGeTe_3 monolayers. *npj Comput. Mater.* **4**, 57 (2018).
- [58] L.-C. Zhang, F. Zhu, D. Go, F. R. Lux, F. J. dos Santos, S. Lounis, Y. Su, S. Blügel, Y. Mokrousov, Interplay of Dzyaloshinskii-Moriya and Kitaev interactions for magnonic properties of Heisenberg-Kitaev honeycomb ferromagnets. *Phys. Rev. B* **103**, 134414 (2021).
- [59] C. Xu, J. Feng, M. Kawamura, Y. Yamaji, Y. Nahas, S. Prokhorenko, Y. Qi, H. Xiang, L. Bellaiche, Possible Kitaev Quantum Spin Liquid State in 2D Materials with $S=3/2$. *Phys. Rev. Lett.* **124**, 087205 (2020).
- [60] A. Mook, J. Henk, I. Mertig, Magnon Hall effect and topology in kagome lattices: A theoretical investigation. *Phys. Rev. B* **89**, 134409 (2014).

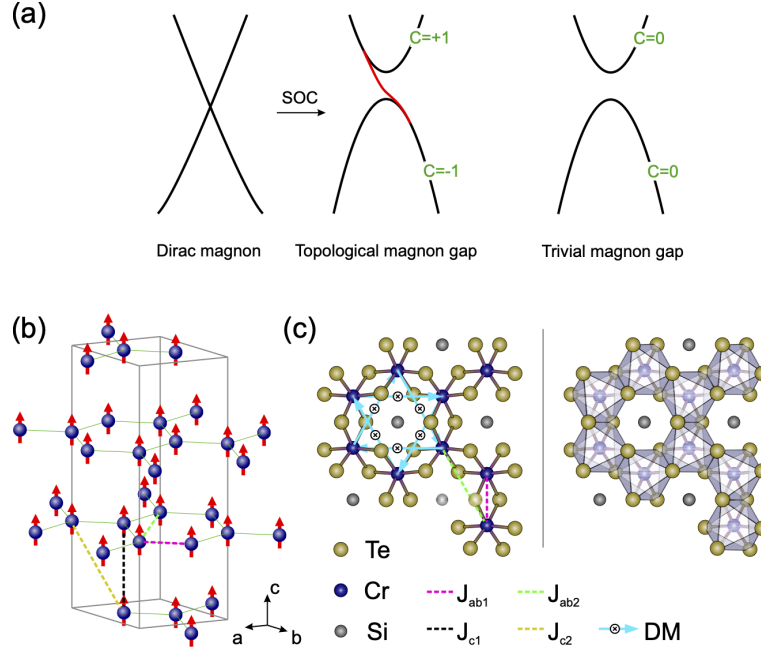


Fig. 1. Schematic of the trivial and topological magnon bands, and of the magnetic and atomic structures of CrXTe_3 . (a) Schematic of the band dispersion for a Dirac magnon, a topological magnon and a trivial magnon. (b) Magnetic structure of CrSiTe_3 . In the ab -plane, the Cr atoms form a honeycomb lattice represented by the dark blue spheres and green solid lines. The magnetic moments are represented by red arrows. The first and second nearest-neighbor exchange interactions in intra- and inter-planes are represented by purple, green, black and yellow dash lines respectively. (c) View perpendicular to the ab -plane showing the honeycomb network of CrSiTe_3 . The honeycomb network is caged by the edge-sharing octahedra composed of Te atoms and Si-Si dimers located in the center. The light blue arrows represent the bond directions of the DM interactions between the second nearest-neighbor Cr atoms, and all the DM vectors share a common sign along the c axis.

| unit (meV) | J_{ab1} | J_{ab2} | J_{c1} | J_{c2} | \vec{D}_{ij} |
|-------------------|-----------|-----------|----------|----------|----------------|
| CrSiTe_3 | 1.49 | 0.15 | 0.07 | 0.06 | (0, 0, 0.12) |
| CrGeTe_3 | 2.73 | 0.33 | 0.10 | 0.08 | (0, 0, 0.32) |

TABLE I. Spin Hamiltonian parameters. The values of exchange interactions including the DM interactions are listed together for both CrSiTe_3 and CrGeTe_3 . The value of the 2nd-NN DM-vector was chosen to reproduce the experimental spin-wave dispersion. The units of the parameters indicated here is meV. The single-ion anisotropy is fixed to 0.01 meV.

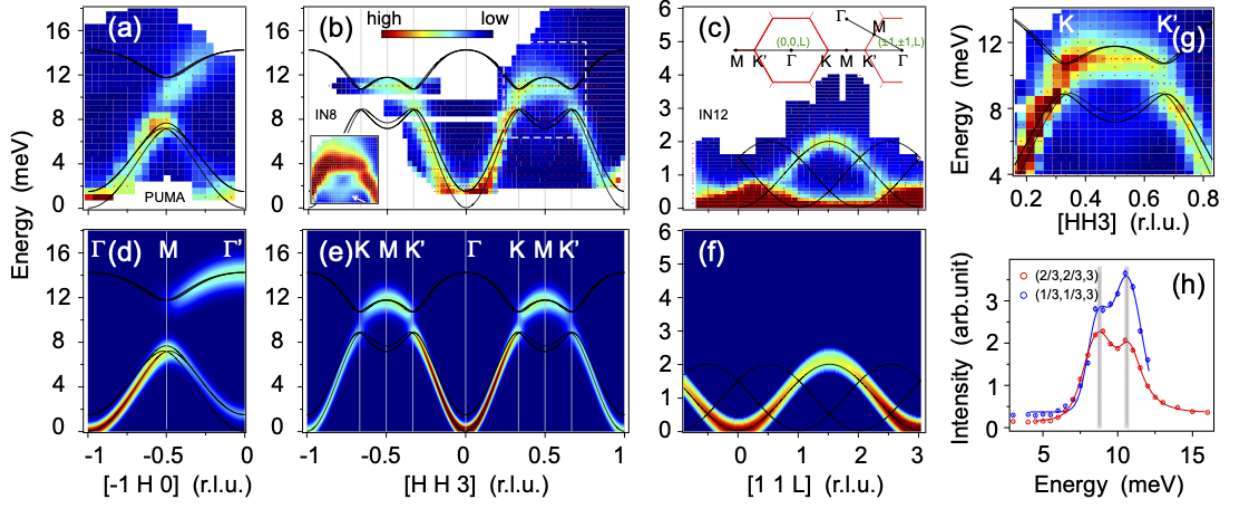


Fig. 2. Spin-wave excitations in CrSiTe₃. (a-c) Energy- and momentum-resolved neutron scattering intensity maps of magnons in CrSiTe₃ along the high-symmetry directions measured at the thermal neutron triple-axis spectrometer PUMA and IN8, and at the cold neutron triple-axis spectrometer IN12, respectively. The black solid lines are the calculated magnon dispersion curves based on the parameters of Heisenberg-DM model presented in this paper. The inset in (b) is a contrast adjusted plot for the dashed rectangle part to make the acoustic branch easy to see. The inset in (c) shows the exact scan paths in the reciprocal space. (d-f) Calculated magnon spectra intensity maps for (a-c) respectively. The calculated spectra are convolved with an energy resolution of 1 meV to compare with the experimental data. (g) Zoom-in plot of the magnon spectra from (b) near the *K* points. (h) Energy scans of magnon density of states at the *K* points. The solid lines are the two-peak Gauss fitting results, and the fitted peak positions and error bars are indicated by the vertical dash lines with gray shadow.

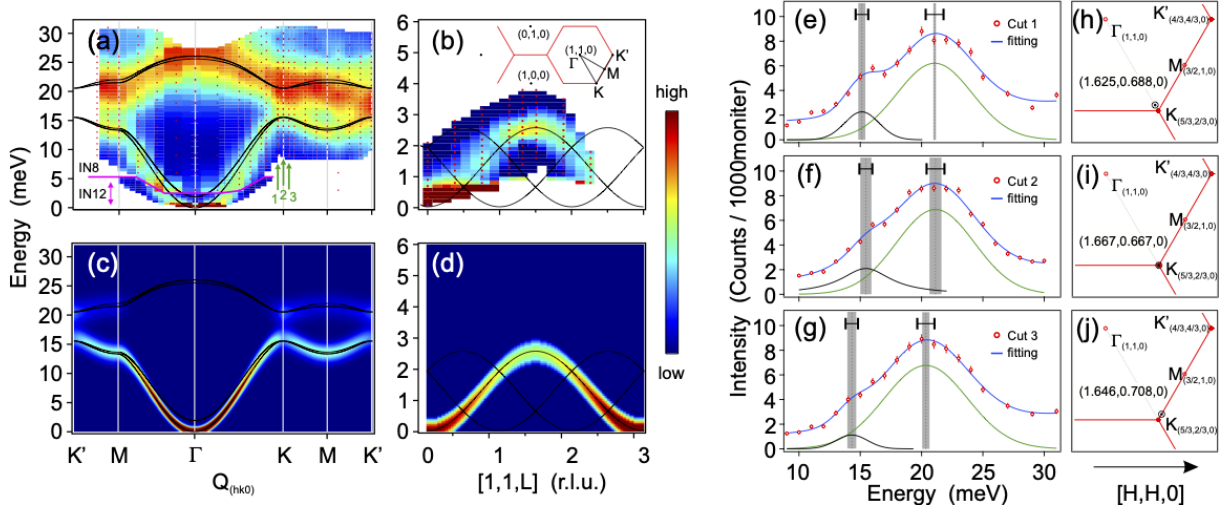


Fig. 3. Spin-wave excitations in CrGeTe₃. (a,b) Energy- and momentum-resolved neutron scattering intensity maps of magnon in CrGeTe₃ along the high-symmetry directions measured at IN8 and IN12, respectively. Black solid lines are the calculated magnon dispersion curves. Inset in (b) shows the projected BZ with high-symmetry points and the scan paths in the experiments. (c,d) The corresponding calculated magnon spectra intensity maps for (a,b) by using the 2nd-NN DM interaction model. The calculated spectra are convolved with an energy resolution of 1 meV to compare with experimental data. (e-g) The line profiles of constant-Q energy scan at the positions of 1,2,3 marked by the green arrows in (a) near the K point $Q = (5/3, 2/3, 0)$. The solid lines are the multi-peak Gauss fitting results. The peak positions and the errors are indicated respectively by the dash lines and the gray shadows, the corresponding energy resolutions are represented by the black horizontal bar with caps. (h-j) The actual Q positions of the Cut 1,2,3 are marked by black circles with center dots in the reciprocal space. The red solid lines are the BZ boundaries.

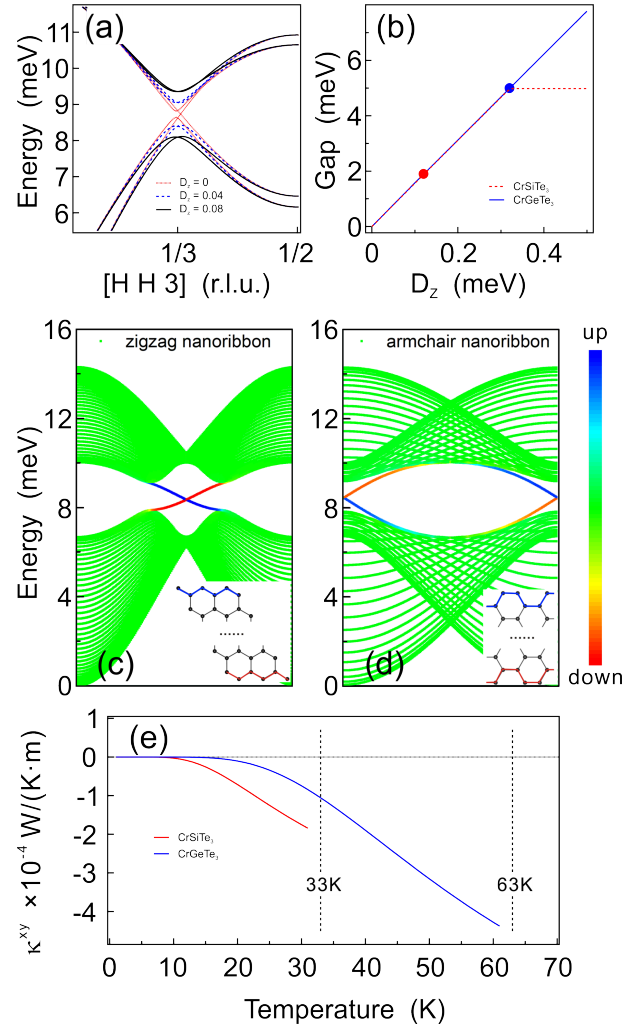


Fig. 4. The impact of the DM interaction on the magnon dispersion. The magnon dispersions of CrSiTe₃ with different DM interaction strength are compared in (a). (b) The relationships between the opened global band gap and the strength of the DM interaction, the red and blue filled circles correspond to the values extracted from the magnon bands. (c,d) The edge states of the monolayer CrSiTe₃ for the respective zigzag and armchair nanoribbon. The color scale represents the weight of the magnonic wave function along the slab. (e) Temperature dependence of the topological thermal Hall conductivity of CrSiTe₃ and of CrGeTe₃ in the ferromagnetic ordered phases.

Supplemental materials: Topological magnon insulators in two-dimensional van der Waals ferromagnets CrSiTe₃ and CrGeTe₃: towards intrinsic gap-tunability

Fengfeng Zhu, Lichuan Zhang, Xiao Wang, Flaviano José dos Santos, Junda Song, Thomas Mueller, Karin Schmalzl, Wolfgang F. Schmidt, Alexandre Ivanov, Jitae T. Park, Jianhui Xu, Jie Ma, Samir Lounis, Stefan Blügel, Yuriy Mokrousov, Yixi Su, Thomas Brückel

VI. DATA ANALYSIS

A. X-ray diffraction, magnetic properties and neutron scattering

The lattice parameter $c = 20.681(75)$ Å for CrSiTe₃ and $c = 20.603(99)$ Å for CrGeTe₃ at room temperature extracted from XRD (in Fig.S1[(a),(b)]) is quite consistent with the previous results [52–54]. From the temperature dependence of the magnetic susceptibility (shown in Fig.S1[(c),(d)]), the ferromagnetic transitions can clearly be observed at $T_c \approx 33$ K for CrSiTe₃ and $T_c \approx 63$ K for CrGeTe₃, respectively. In the insets of Fig.S1[(c),(d)], the isothermal magnetization ($M - H$) curves show small magnetic anisotropies, and the magneto-crystalline anisotropy is extracted as 0.09 meV for CrSiTe₃ and 0.02 meV for CrGeTe₃, respectively. In Fig.S1[(e),(f)], the phase transition is also observed from the temperature dependence of the (1,1,0) magnetic Bragg peak for both CrSiTe₃ and CrGeTe₃. The temperature dependence of the order parameter were fitted with the power law equation $I = I_0 + A(1 - \frac{T}{T_N})^{2\beta}$, the fitted transition temperatures are about 33 K for CrSiTe₃ and 63 K for CrGeTe₃, which are in a good agreement with our magnetization results. The critical exponents are extracted as $\beta = 0.151(3)$ for CrSiTe₃ and $\beta = 0.201(7)$ for CrGeTe₃.

With polarized neutron diffraction, we can easily determine the directions of the ordered magnetic moments, because the sign of polarized neutrons can only be flipped when there exists a non-zero component of magnetic moments perpendicular to the polarization of the neutron beam \mathbf{P} and the scattering wave vector \mathbf{Q} . Due to a favorable situation related to the ferromagnetic domains in this sample, no neutron depolarization was noticed for the polarized measurements in the ferromagnetic state. As shown in Fig.S2, 2D \mathbf{Q} -maps in the (H,K,0) and (H,H,L) planes of reciprocal space at three different polarization modes were measured at 4 K. The diffraction patterns of x and y polarization for the respective spin-flip and non-spin-flip channels (Fig.S2(a-d)) are basically the same in the (H,K,0) scattering plane, and all the nuclear and magnetic diffraction peaks relocated on the same position in the center of Brillouin zone, which indicates its ferromagnetic character and that the ferromagnetic moment has a non-zero component along the z directions at least. For the z polarization, there are no diffraction peaks observed in the spin-flip channel but the same diffraction pattern as in the previous xy polarizations of the non-spin-flip channel, as shown in Fig.S2[(e),(f)], which confirms that the ordered ferromagnetic moments are aligned exclusively along the c axis. The absence of the (0,0,3n) magnetic reflections in the x spin-flip channel compared to the x non-spin-flip channel (shown in Fig.S2(g)), also indicates the magnetic moments are aligned along the c axis.

For the measurements of spin-wave excitations, the full width at half maximum of CrSiTe₃ is much smaller than that of CrGeTe₃. For CrSiTe₃ single crystals, due to the large size and thickness, we used only 2 single crystals and the FWHM of the co-aligned sample turns out to be only 1.4° in the rocking curve scan at IN8, as shown in Fig.S3(a). However, for CrGeTe₃ single crystals, their usual dimension is about $2 \text{ mm} \times 2 \text{ mm} \times 0.5 \text{ mm}$, so we co-aligned about 0.8 g samples on 5 horizontal aluminum plates and about 0.6 g samples on 3 vertical aluminum plates for the experiments with (H,K,0) and (H,H,L) as scattering planes, respectively. The corresponding FWHM of the (H,K,0) orientated CrGeTe₃ sample is about 3.52° (shown in Fig.S3(b)).

B. Constant-energy mapping around the K points

To gain more information about the the magnon band dispersion in the vicinity of the K points, we have also very carefully measured the constant-energy scan contour maps in the (H,K,0) reciprocal plane with various energy transfers, as shown in Fig.S4(a-h). The energy transfers were selected from 7.5 meV to 11 meV with a step of 0.5 meV to cover the whole range of the gap opening at the K points. In Fig.S4(q), a 2D reciprocal space map with BZ boundaries and high-symmetry points in (H,K,0) is shown, and the measured regions of the constant-energy slices in \mathbf{Q} space are indicated by the light blue hexagons. However, the spectral function (or dynamic structure factor) is strongly dependent on the momentum transfer, causing intensity enhancement or suppression in some specific parts of the contour maps. According to the previously calculated spectral function for the honeycomb ferromagnet with DM interactions, the magnon shows a shorter lifetime in the acoustic mode on one side of the K point and, in the optical mode on the opposite side of K , which is consistent with the antisymmetric intensity distribution that we observed

in Fig.S4(a-h). From the constant-energy slices, the 2D projected magnon “cone” is observed to become weaker and smaller towards the gap energy, and become larger again by increasing energy transfers. In between, for example at $E = 9.5$ meV, only discrete spots with weak intensity can be seen at the K points, as shown in Fig.S4(e).

Although the existence of a gap opening is almost clear by observing the intensity change of the constant-energy contours, it is not rigorous and convincing enough, given that similar constant-energy contours were also observed in the topological Dirac magnon material CoTiO_3 where there exists no gap at the K points [17]. To exclude the involvement of the Dirac magnon, further detailed constant- Q energy scans at various K points are quite necessary. In Fig.S4(r), the energy-scan line profiles were extracted at three K points [highlighted by green circles in Fig.S4(q)] with different momentum transfers, and all of them show two peaks located at around 8.7 meV and 10.7 meV, which clearly indicate a 2 meV gap opening at around 9.5 meV. Due to the limited energy resolution of ~ 1.3 meV that is also comparable to the gap size, the in-gap intensity is not exactly zero in our experimental configuration. By applying a convolution of the instrument energy resolution, similar constant-energy patterns including the discrete spot-shaped contours at $E = 9.5$ meV can be very well reproduced in our simulations, as shown in Fig.S4(i-p).

C. Determination of the magnon gap at the Brillouin zone center

We tried to measure the spin wave gap at the Γ point by using one of the best cold neutron triple-axis spectrometers, IN12, but we failed although the energy resolution and background level were quite good. Unlike CrI_3 , the anisotropy in both CrSiTe_3 and CrGeTe_3 is very small [32, 34, 35], it is really hard to resolve it directly from our low energy scan data. To give out a reference value of the spin wave gap, we carefully measured the low energy magnon bands along the high-symmetry directions at 2 K. In the color map of Fig.S5(a), the magnon bands of CrGeTe_3 below 15 meV were measured at IN12 with $k_f = 1.7 \text{ \AA}^{-1}$, and the magnon bands above 15 meV were measured with $k_f = 2.8 \text{ \AA}^{-1}$. Fig.S5(b) shows the corresponding calculated dispersion curves of the same Q path as in Fig.S5(a) by using the fitted exchange parameters in the Heisenberg-DM model. In the vicinity of the Γ point at low energy, the magnon bands dispersions along $\Gamma - M$ and $\Gamma - K$ can be both fitted by the parabolic equation under the long-wave approximation. Here, for the quadratic fitting, the Gauss fitted peak positions of the measured magnon bands below 5 meV were included, as shown in the red rectangular frame of Fig.S5(c). The fitting results were shown in the form of the energy as a linear function of the squared moment transfer Q , and the fitted gap size at the Γ point is about 0.0097 meV but with a very large error of 0.183 meV, which indicates the gap of CrGeTe_3 is rather small and really hard to resolve by triple-axis spectroscopy.

For the same reason, the magnon band dispersions of CrSiTe_3 and CrGeTe_3 along the $[0\ 0\ L]$ direction were also fitted to gain a reference value of the spin wave gap at the Γ point, as shown in Fig.S6. Given the magnetic structure is ferromagnetic in both the intralayers and also the vdW interlayers, we can treat every three ABC-stacked ferromagnetic Cr^{3+} as a single imaginary spin with $S = 3/2 \times 3$, so the spin wave dispersion along the c axis that is concerned here can be approximately described by using a one-dimensional ferromagnetic model with an effective nearest-neighbor ferromagnetic exchange interaction \tilde{J} :

$$H = -\tilde{J} \sum_i (S_i^x S_{i+1}^x + S_i^y S_{i+1}^y + \Delta S_i^z S_{i+1}^z) - A_{zz} \sum_i (S_i^z)^2, \quad (\text{S1})$$

where Δ and A_{zz} denote the exchange and single-ion anisotropy, respectively. In the case $\Delta = 1$, the exchange interaction reduces to the isotropic Heisenberg interaction. At low temperatures ($k_B T \ll \tilde{J}$), the perturbations of the ground state are very small, so we can ignore the high-order terms and just keep the ground-state energy term and quadratic terms in bosonic operators. Finally, the ferromagnetic magnon dispersion can be wrote as

$$\epsilon_k = 2\tilde{J}S(\Delta - \cos(kc)) + 2A_{zz}S, \quad (\text{S2})$$

where c is the lattice constant along the z direction. The gap at the Brillouin zone center Γ point is expressed as $2\tilde{J}S(\Delta - 1) + 2A_{zz}S$. The band dispersions in Fig.S6 were fitted by using Eq.S2, and the effective exchange interactions \tilde{J} were determined as 0.11(1) and 0.16(2) meV for CrSiTe_3 and CrGeTe_3 respectively. From the fitting results, we failed to get the anisotropy gap size because of the extremely small magnetic anisotropy in CrXTe_3 . To give an idea of how small the single-ion anisotropy is, we set $\Delta = 1$, namely Heisenberg interaction, and the single-ion anisotropy is estimated as $A_{zz} < 0.0018$ meV for CrSiTe_3 and $A_{zz} < 0.020$ meV for CrGeTe_3 . The small single-ion anisotropy can basically be neglected, compared to the large in-plane exchange interactions J_{ab} . However, for the overall magnon band fitting (e.g. in Fig.S5(b)), we symbolically set the single-ion anisotropy A as 0.01 meV for the Hamiltonian in Eq.S1.

VII. SPIN HARMILTONIAN

A. Heisenberg-DM model

For the CrXTe₃, although the DM interaction will cancel because of the space inversion between the nearest-neighbor Cr atoms, the second nearest-neighbor interaction, the space inversion symmetry is actually broken in a honeycomb lattice, leading to a non-zero DM interaction. Although the Te atoms may appear to have the strongest SOC in CrXTe₃, the magnitude of the DM interaction is more likely determined by the competition of one Cr atom and two Si/Ge atoms on two sides of the second nearest-neighbor Cr-Cr bond. Here we use LSWT to calculate the magnon spectra of CrXTe₃, starting from the generalized Heisenberg model [40],

$$H = \sum_{i < j} \mathbf{S}_i^\dagger \hat{\mathbf{J}}_{ij} \mathbf{S}_j, \quad (\text{S3})$$

where the interaction tensor between the lattice sites i and j

$$\hat{\mathbf{J}}_{ij} = \begin{pmatrix} J_{ij}^x & D_{ij}^z & -D_{ij}^y \\ -D_{ij}^z & J_{ij}^y & D_{ij}^x \\ D_{ij}^y & -D_{ij}^x & J_{ij}^z \end{pmatrix} \quad (\text{S4})$$

includes the symmetric exchange \mathbf{J}_{ij} and the antisymmetric off-diagonal DM interaction terms \mathbf{D}_{ij} , caused by the spin-orbit coupling. The DM interaction vector is defined as $\mathbf{D}_{ij} = (D_{ij}^x, D_{ij}^y, D_{ij}^z)$. Based on the symmetry and the Moriya's rule, the direction of the DM interaction vector is determined as out of plane. Similar to earlier works [27], we include five Heisenberg exchange interactions in total, three in the intra-layers and two between the inter-layers, with their numerical values listed in Table I.

According to the LSWT, the Holstein-Primakoff transformation [55] is adopted for the quantum spin operators. Followed by the Fourier transformation for the boson operators, the Hamiltonian matrix in momentum space is obtained. Then the eigenvalue and eigenvector, namely the magnon band dispersion can be extracted through diagonalizing the matrix. As we expected, the band opens a gap at the K point which is consistent with our experimental results.

B. Heisenberg-Kitaev model

The Kitaev interaction is introduced to understand the magnetic behaviors that are close to quantum spin liquids in some S=1/2 honeycomb lattices with edge-sharing octahedra compounds, e.g., Na₂IrO₃, α -RuCl₃ [43, 56]. For the S=3/2 systems, like CrXTe₃, the Kitaev-type exchange interaction may also exist, and recent theoretical works [57] have proposed to realize the Kitaev quantum spin liquid state in CrGeTe₃ by applying proper in-plane strain. As shown in the schematic of Fig.S7(a), the nearest Cr-Cr pairs are proposed to have three bond-dependent Ising exchange interactions in the local $\{\alpha\beta\gamma\}$ coordinate bases for the Kitaev model. For simplicity, here we first discuss the Kitaev model in the perfect orthogonal $\{\alpha\beta\gamma\}$ coordinate bases. The Heisenberg-Kitaev Hamiltonian can be expressed as:

$$H = - \sum_{i < j} J_{ij} \mathbf{S}_i \cdot \mathbf{S}_j - \sum_{\langle i,j \rangle_\nu} K^\nu S_i^\nu S_j^\nu - A_{zz} \sum_i (S_i^z)^2, \quad (\text{S5})$$

where the first term is the Heisenberg exchanges term and the second term represents the nearest neighbour bond-dependent Kitaev interaction with $K^\alpha = K^\beta = K^\gamma = K$. To obtain the final magnon dispersion, the Kitaev term in the Hamiltonian expressed by the local $\{\alpha\beta\gamma\}$ basis can be converted into the global $\{xyz\}$ coordinate in advance to apply the Holstein-Primakoff transformation and Fourier transformation, and then the total Hamiltonian can be rewrote in momentum space by bosonic operators. According to the linear-spin-wave theory, we can ignore the high-order terms and just keep the ground-state energy term and the linear terms which contain the magnon relation. By fitting the experimental results with the model, we can easily obtain the exchange parameters. Comparing to the previous Heisenberg-DM model, the DM term is just replaced by the Kitaev term, and also up to five isotropic Heisenberg interactions are included for CrXTe₃. To make the calculated magnon bands consistent with the measured band dispersion, the optimized Kitaev interaction parameters are quite large comparing to their nearest-neighbor Heisenberg interaction for both CrSiTe₃ and CrGeTe₃. The corresponding exchange parameters for CrXTe₃ are listed

in Table.S1. As shown in Fig.S8, the magnon band of CrSiTe₃ reproduced by the Heisenberg-Kitaev model is quite similar to the result of the pure Heisenberg model but opens a gap in the vicinity of the K point like that of the Heisenberg-DM model.

However, it is important to realize that the $\{\alpha\beta\gamma\}$ basis is not perfectly orthogonal in CrXTe₃, the interangle between the local $\{\alpha\beta\gamma\}$ basis vectors is about 93.6° and 100.1° for CrSiTe₃ and CrGeTe₃ respectively. As shown in the schematic picture of Fig.S7(b), the local $\{\alpha\beta\gamma\}$ basis vectors tilt from the z axis towards the xy plane by an angle θ , and only when $\theta = \theta_0 \approx 54.74^\circ$, namely $\tan\theta = \sqrt{2}$, the $\{\alpha\beta\gamma\}$ basis becomes perfectly orthogonal[58]. Here in our paper, we take θ as 57.28° and 62.26° from the experimental refined atomic structures of CrSiTe₃ and CrGeTe₃ respectively. The imperfection of θ will yield non-zero off-diagonal components when the exchange matrix is converted into the orthogonal $\{\alpha'\beta'\gamma'\}$ basis and eventually induce an extra exchange anisotropy along the global z axis. Three general Kitaev interaction matrices in a local $\{\alpha\beta\gamma\}$ basis can be expressed as:

$$\begin{pmatrix} K^\alpha & & \\ & 0 & \\ & & 0 \end{pmatrix}, \quad \begin{pmatrix} 0 & & \\ & K^\beta & \\ & & 0 \end{pmatrix}, \quad \begin{pmatrix} 0 & & \\ & 0 & \\ & & K^\gamma \end{pmatrix}, \quad (\text{S6})$$

and in the orthogonal $\{\alpha'\beta'\gamma'\}$ basis, they can be rewritten as:

$$\begin{pmatrix} A^2 & AB & AB \\ AB & B^2 & B^2 \\ AB & B^2 & B^2 \end{pmatrix} \cdot \frac{K^\alpha}{C^2}, \quad \begin{pmatrix} B^2 & AB & B^2 \\ AB & A^2 & AB \\ B^2 & AB & B^2 \end{pmatrix} \cdot \frac{K^\beta}{C^2}, \quad \begin{pmatrix} B^2 & B^2 & AB \\ B^2 & B^2 & AB \\ AB & AB & A^2 \end{pmatrix} \cdot \frac{K^\gamma}{C^2}, \quad (\text{S7})$$

where $A = 2 \sin\theta \cos\theta_0 + \cos\theta \sin\theta_0$, $B = -\sin(\theta - \theta_0)$ and $C = 3 \sin\theta_0 \cos\theta_0$. Especially when $\theta = \theta_0$, then we have $B = 0$ and $A = C$, the Eq.S7 is immediately degenerated into the simple form the same as the Eq.S6. However for CrSiTe₃ and CrGeTe₃ here, the off-diagonal term is non-zero due to $\theta \neq \theta_0$, hence for example one of the Kitaev matrices will representatively be

$$\begin{pmatrix} 0.998 & -0.032 & -0.032 \\ -0.032 & 0.001 & 0.001 \\ -0.032 & 0.001 & 0.001 \end{pmatrix} \cdot K^\alpha, \quad \begin{pmatrix} 0.983 & -0.092 & -0.092 \\ -0.092 & 0.009 & 0.009 \\ -0.092 & 0.009 & 0.009 \end{pmatrix} \cdot K^\alpha. \quad (\text{S8})$$

In the orthogonal $\{\alpha'\beta'\gamma'\}$ basis, the general Heisenberg-Kitaev Hamiltonian can be expressed as:

$$\begin{aligned} H = & - \sum_{i < j} \tilde{J}_{ij} \mathbf{S}_i \cdot \mathbf{S}_j - \sum_{\langle i,j \rangle_\nu} \tilde{K}^\nu S_i^\nu S_j^\nu - \sum_{\langle i,j \rangle_{\mu\nu}} \Gamma_1 (S_i^\mu S_j^\nu + S_i^\nu S_j^\mu) \\ & - \sum_{\langle i,j \rangle_{\lambda\mu\nu}} \Gamma_2 (S_i^\lambda S_j^\mu + S_i^\mu S_j^\lambda + S_i^\lambda S_j^\nu + S_i^\nu S_j^\lambda) - A_{zz} \sum_i (S_i^z)^2, \end{aligned} \quad (\text{S9})$$

where $\Gamma_1 = \frac{B^2}{C^2}K$, $\Gamma_2 = \frac{AB}{C^2}K$, $\tilde{K}^\nu = \frac{(A^2 - B^2)}{C^2}K$ and $\tilde{J}_{ij} = J_{ij} + \frac{B^2}{C^2}K$ for the nearest-neighbor exchange interactions, $\tilde{J}_{ij} = J_{ij}$ for others, and (λ, μ, ν) is any permutation of orthogonal basis vector's indexes $(\alpha', \beta', \gamma')$.

Although the non-zero off-diagonal terms in the matrix looks small, but here they will create an quite large negative component (e.g. CrSiTe₃: -0.7 meV, CrGeTe₃: -5.7meV) on the magnon gap at the Brillouin center and make the energy eigenvalues become imaginary unless an extra considerable anisotropy can be introduced to cancel it out. If so, either the anisotropy of the exchange interaction or the single ion anisotropy should be very strong. However, as we known from the magnetization and the critical behavior, the magnetic anisotropy in CrXTe₃ is quite small actually. Even if the magnon dispersion can be reproduced very well when the bond-dependent Kitaev interactions are assumed to be perfectly orthogonal, it is still difficult to understand the huge difference of the strength of the Kitaev interaction between CrSiTe₃ and CrGeTe₃, since the Kitaev interaction mainly arise from the heavy ligands (namely, Te of CrXTe₃) [57, 59]. We can not completely exclude the existence of the Kitaev interaction, but comparing to the previous DM model, the Heisenberg-Kitaev model is unlikely a proper model to describe the exchange interactions in this system at least.

VIII. MAGNON BAND TOPOLOGY

A. Berry curvature and Chern number

Formulating semiclassical equations of motion for magnon wave packets [60], which include the anomalous velocity leads to a non-zero Berry curvature. We generally define the Berry curvature field associated with the n^{th} magnon band as

$$\Omega_{n\mathbf{k}} = i \sum_{m \neq n} \frac{\langle \Psi_{n\mathbf{k}} | \partial_{\mathbf{k}} H(\mathbf{k}) | \Psi_{m\mathbf{k}} \rangle \times \langle \Psi_{m\mathbf{k}} | \partial_{\mathbf{k}} H(\mathbf{k}) | \Psi_{n\mathbf{k}} \rangle}{(\epsilon_{n\mathbf{k}} - \epsilon_{m\mathbf{k}})^2}, \quad (\text{S10})$$

where $\partial_{\mathbf{k}} H(\mathbf{k})$ denotes the gradient of the Hamiltonian in momentum space. $\epsilon_{m\mathbf{k}}$ and $\epsilon_{n\mathbf{k}}$ are the magnonic eigenvalues.

Based on this Berry curvature, we can classify the topology of the n^{th} magnon branch using Chern number:

$$C(P) = \frac{1}{2\pi} \int_P \Omega(\mathbf{k}) \cdot \tilde{\mathbf{n}} dP, \quad (\text{S11})$$

where P is a two-dimensional slice of the BZ and $\tilde{\mathbf{n}}$ is its normal vector. In our calculation, the $\tilde{\mathbf{n}}$ is selected perpendicular to the xy plane. As the lowest three branches cross with each other, the lower three branches are sum together.

The Berry curvature distribution of bulk CrGeTe₃ in the first BZ is shown in Fig.S9(a,b). The Chern number of the lowest three branches is -3 and the Chern number of the highest three branches is $+3$. If we ignore the interlayer interaction, we can easily use the monolayer system to characterize the topological properties of the system, and the corresponding Berry curvature is shown in Fig.S9(c,d) with the Chern number -1 for the lowest branches. From the figure, almost the same Berry curvature distribution can be obtained. Compared to the intralayer interaction, the interlayer interaction is weaker and the DM interaction only exist among intralayer. In CrXTe₃, each layer contributes one optical and acoustic branches. The interlayer interaction splits the three degenerate bands but influence little on their topological properties.

B. Edge states and thermal Hall conductivity

To simplify the calculation, the monolayer CrXTe₃ is utilized to study the edge states. Here, the color scale of the bands in the main text Fig.4 is calculated based on the following equation:

$$LW(\mathbf{k}, j) = \sum_i \phi^{i*}(\mathbf{k}, j) \phi^i(\mathbf{k}, j) (R_z^i - 0.5), \quad (\text{S12})$$

where \mathbf{k} is the reciprocal space vector, j denotes the band index, i numbers the magnetic atom, and R_z^i represents the normalized position for atom i along the z -axis. $\phi^i(k, j)$ is the components of the right eigenstates of j at the magnetic atom i .

Given the nontrivial topology, the topological magnon edge states can contribute to the transverse thermal Hall voltage under an applied longitudinal temperature gradient [18, 24–26, 60], namely the topological thermal Hall effect.

The energy-dependent contribution to the ij 'th Cartesian component of the thermal Hall conductivity tensor $\hat{\kappa}$ can be calculated as

| | J_{ab1} | J_{ab2} | J_{c1} | J_{c2} | K |
|---------------------|-----------|-----------|----------|----------|-----|
| CrSiTe ₃ | 0.4 | 0.2 | 0.08 | 0.065 | 3 |
| CrGeTe ₃ | 0.24 | 0.42 | 0.1 | 0.08 | 6.5 |

TABLE S1. The parameters of the Heisenberg exchange interactions and the Kitaev interactions are listed together for CrSiTe₃ and CrGeTe₃. The local $\{\alpha\beta\gamma\}$ basis is assumed perfectly orthogonal and the single-ion anisotropy is fixed to 0.01 meV. The unit of the parameters is meV.

$$\kappa^{ij}(\epsilon) = \frac{k_B^2 T}{(2\pi)^3 \hbar} \sum_n \int_{\text{BZ}} \delta(\epsilon_{n\mathbf{k}} - \epsilon) C_2(f_n^B) \Omega_n^{ij}(\mathbf{k}) d\mathbf{k}, \quad (\text{S13})$$

where n enumerates the magnon bands, f_n^B is the Bose-Einstein distribution function, which can be expressed as $f_n^B = (e^{\epsilon_{n\mathbf{k}}/k_B T} - 1)^{-1}$, and C_2 is given by

$$C_2(x) = (1+x) \left(\ln \frac{1+x}{x} \right)^2 - \ln^2 x - 2\text{Li}_2(-x), \quad (\text{S14})$$

with Li_2 denoting the dilogarithm function. In our calculation, only the result of transverse thermal Hall conductivity κ^{xy} is shown, as the κ^{xz} and κ^{yz} is zero. The transverse thermal Hall conductivity of the system is then defined as $\kappa^{xy} = \lim_{\mu \rightarrow \infty} \kappa_\mu^{xy}$, where $\kappa_\mu^{xy} = \int_0^\mu \kappa^{xy}(\epsilon) d\epsilon$ is the cumulative thermal Hall conductivity.

From the experimental results, we know that the respective Curie temperature of CrSiTe_3 and CrGeTe_3 are around 30 K and 60 K. The calculated temperature-dependent and energy-dependent thermal Hall conductivity are shown in Fig.S11. For both materials, κ^{xy} is significant enhancement in the energy region close to the band gap, which can be attributed to the distribution of the Berry curvature around the K point. In low temperature only these "topologically-trivial" states are excited according to the Bose-Einstein distribution, leading to the zero platform at very low temperature. Then conductivity increases as the temperature increases. The effect of the DM interaction is shown in Fig.S11(e), from which we can observe that the thermal Hall conductivity increases with the enhancement of the DM Interaction.

The predicted thermal Hall conductivity for CrGeTe_3 reaches the order of 10^{-4} W/Km, which is large enough to be observed in experiment. Furthermore, the DM interaction value is determined by the strength of spin-orbit coupling. Compared to CrGeTe_3 and CrSiTe_3 , CrSnTe_3 and CrPbTe_3 should have even stronger spin-orbit coupling and some recent theoretical studies have demonstrated that the corresponding monolayer system could have a ferromagnetic state with higher Curie temperatures [47, 48]. These materials are thus more likely to have even bigger thermal Hall conductivity than $\text{Lu}_2\text{V}_2\text{O}_7$ [23, 24].

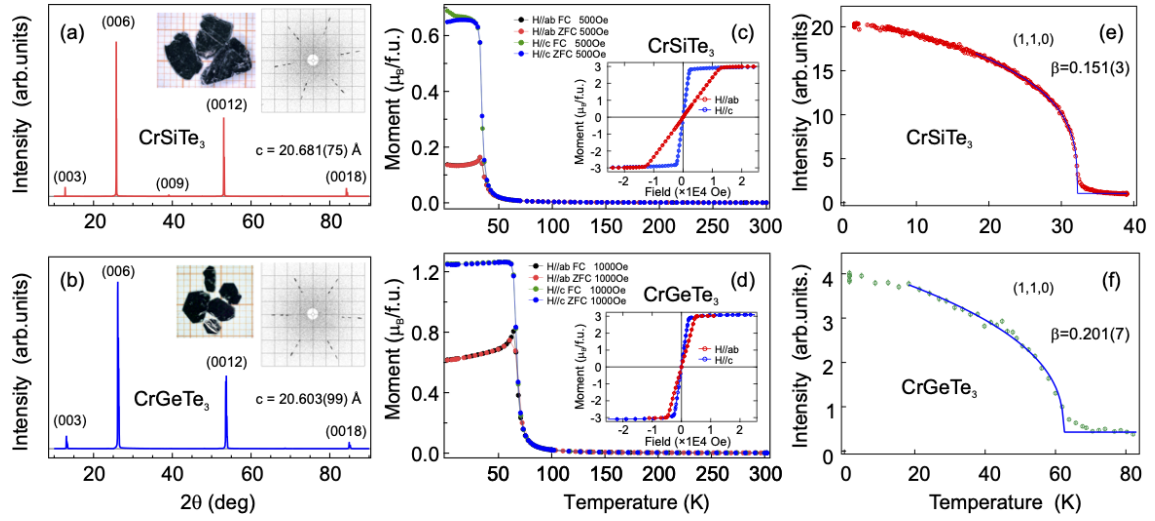


FIG. S1. **X-ray diffraction and magnetic properties of CrXTe₃.** (a,b) X-ray diffraction of single-crystal CrSiTe₃ and CrGeTe₃ at 300 K. The insets are the sample pictures and the corresponding X-ray Laue pattern of the (H,K,0) reciprocal plane. (c,d) ZFC/FC magnetization curves measured under applied magnetic fields along the *c* and *a* axes. Insets show the corresponding magnetization as a function of field at 2 K for *H* || *c* and *H* || *ab*. (e,f) Temperature dependence of the (1,1,0) magnetic Bragg peak intensity of CrSiTe₃ and CrGeTe₃ measured at DNS, MLZ. The solid lines are the fittings of the experimental data in the vicinity of the ferromagnetic transition.

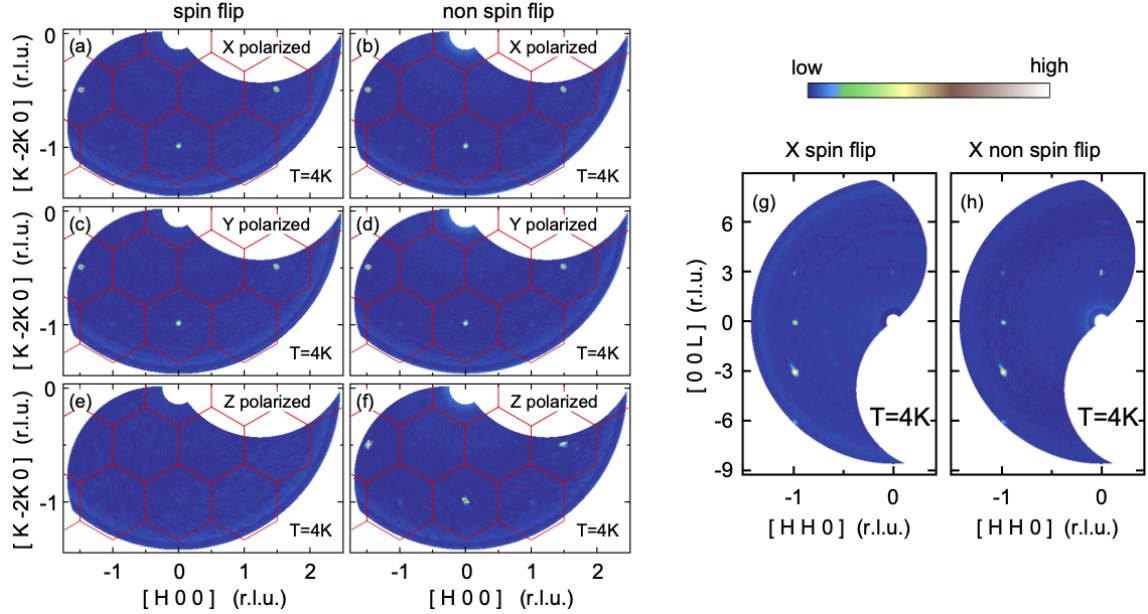
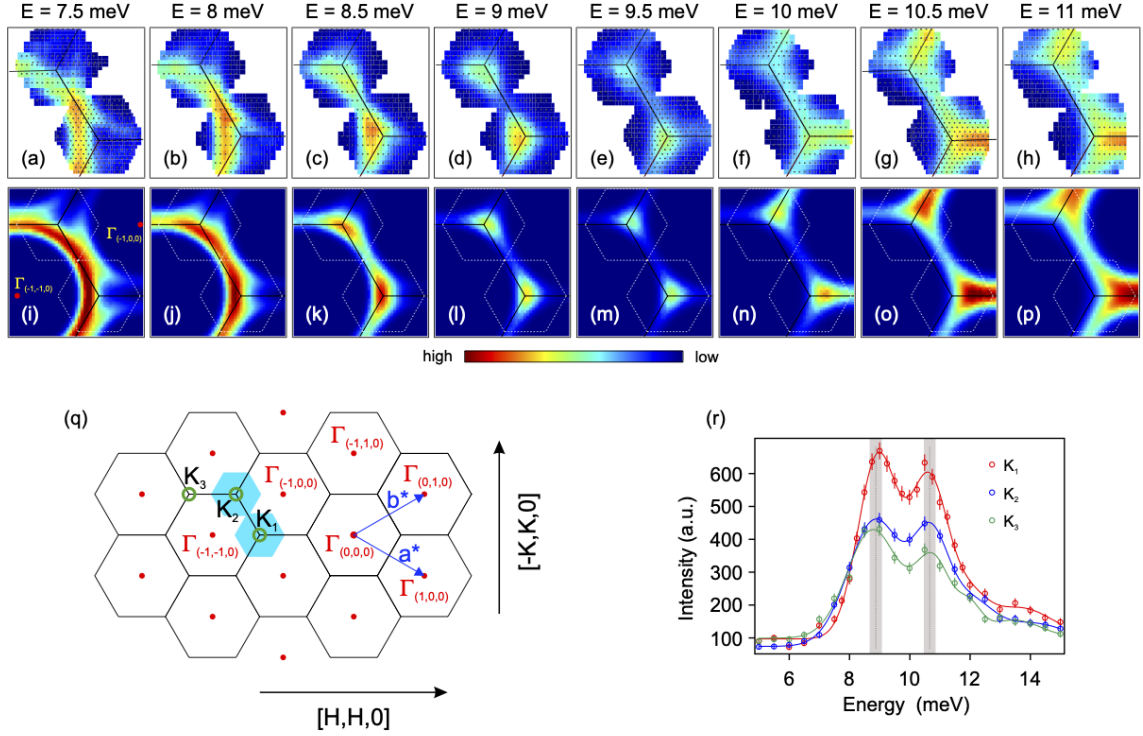
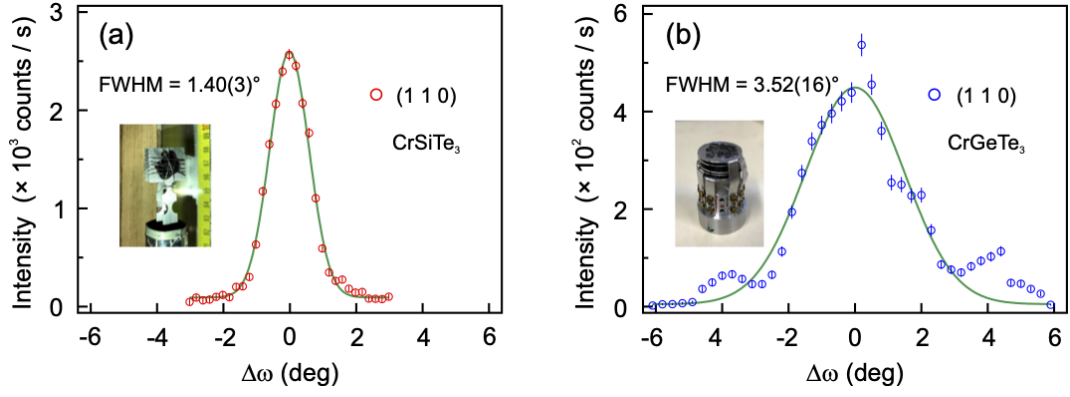


FIG. S2. **Polarized elastic neutron scattering maps.** (a-f) *Q* Maps in the (H,K,0) scattering plane and (g,h) in the (H,H,L) scattering plane measured on CrGeTe₃ at DNS. Red solid lines are the Brillouin zone boundaries.



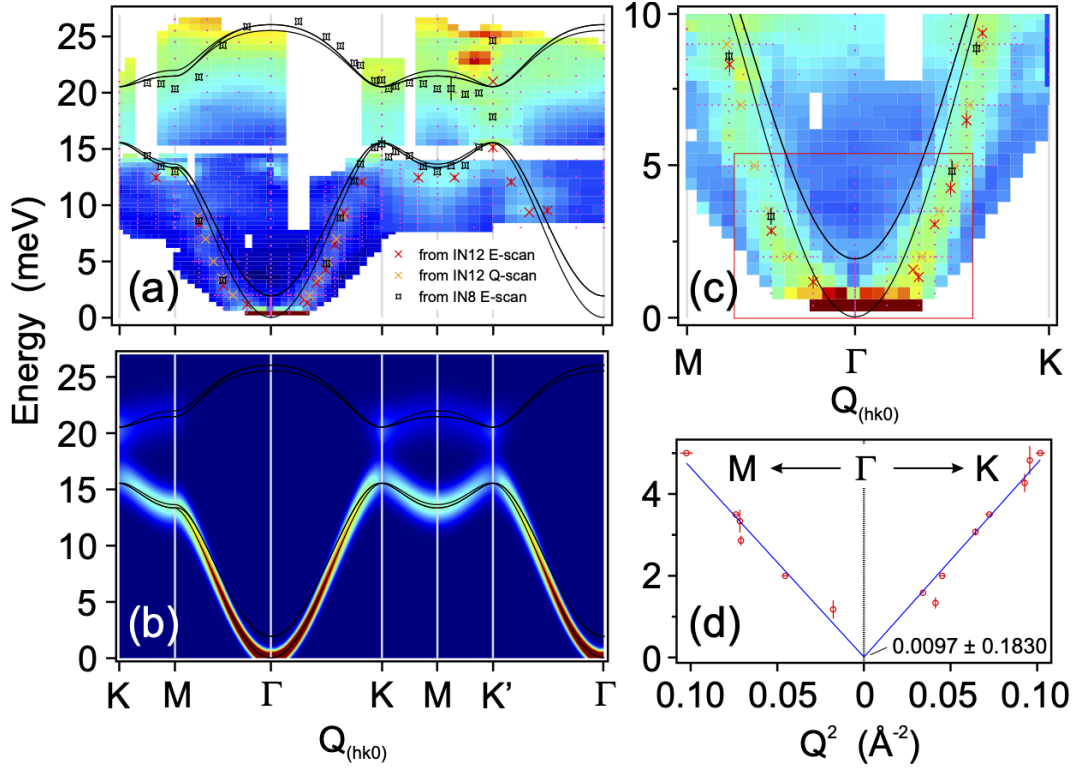


FIG. S5. **The low-energy magnon branches of CrGeTe_3 .** (a) The magnon spectra of CrGeTe_3 measured at the cold neutron triple-axis spectrometer IN12 (with a fixed $k_f = 1.7 \text{ \AA}^{-1}$ and 2.8 \AA^{-1}). The solid lines are the calculated magnon dispersion curves. The isolated crosses and stars are the fitted peak positions of various constant- Q and constant- E scans. (b) The corresponding calculated magnon spectra by using the 2nd-NN DM interaction model. (c) Enlarged plot of the low energy excitations in (a). (d) Quadratic fitting of the magnon band for the low energy parts. Only the peak positions inside the red rectangle in (c) are included in the fitting.

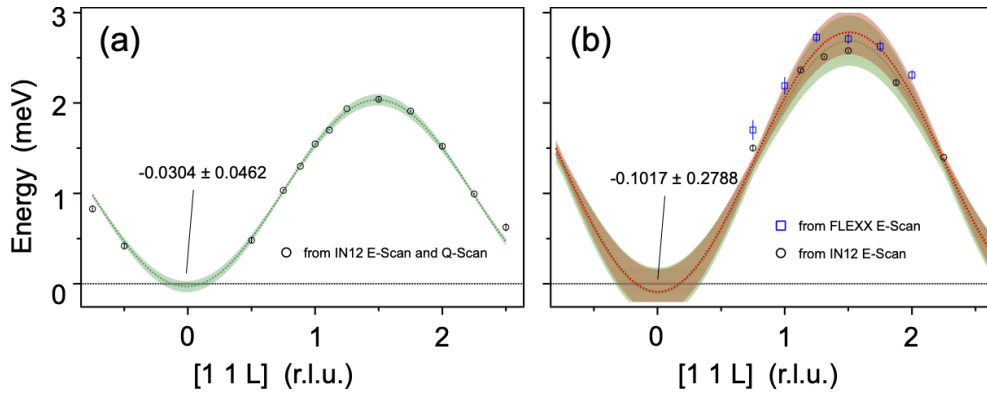


FIG. S6. **Fitting of the magnon dispersion along the $[1,1,L]$ direction.** (a),(b) Cosine-function curve fittings of the respective magnon band dispersion of CrSiTe_3 and CrGeTe_3 along the $[1,1,L]$ direction. The green dashed lines in (a),(b) are the fittings according to the data collected from IN12 ($k_f = 1.7 \text{ \AA}^{-1}$). The red dashed line in (b) is a combined fittings with the restriction in Fig.S5(d) according to all the data of CrGeTe_3 collected from IN12 and FLEXX. The light shading zones represent the confidence interval with a width of 2 standard errors.

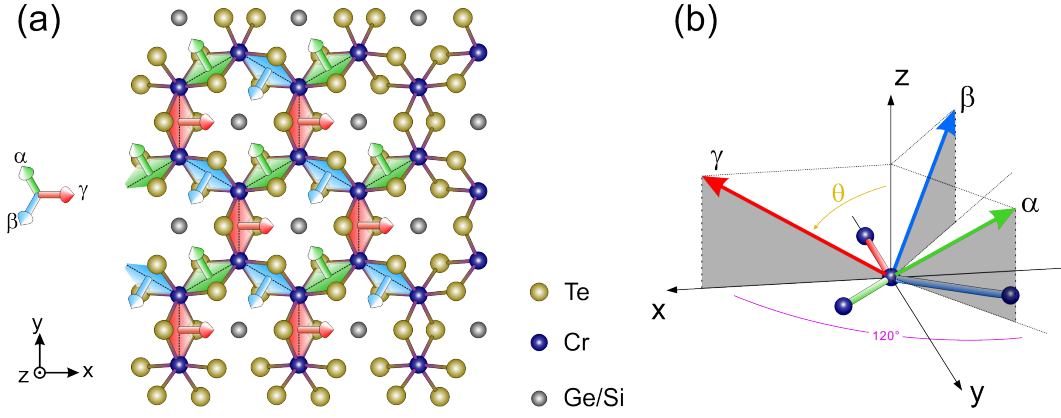


FIG. S7. **The proposed Kitaev model for CrXTe_3 .** (a) Schematic plot for the Kitaev model. The red, blue and green rhombus planes marked with perpendicular arrows are almost orthogonal to each other, which are used to represent 3 different bonds of the Kitaev model. (b) The configuration of the local $\{\alpha\beta\gamma\}$ coordinate in the global $\{xyz\}$ coordinate.

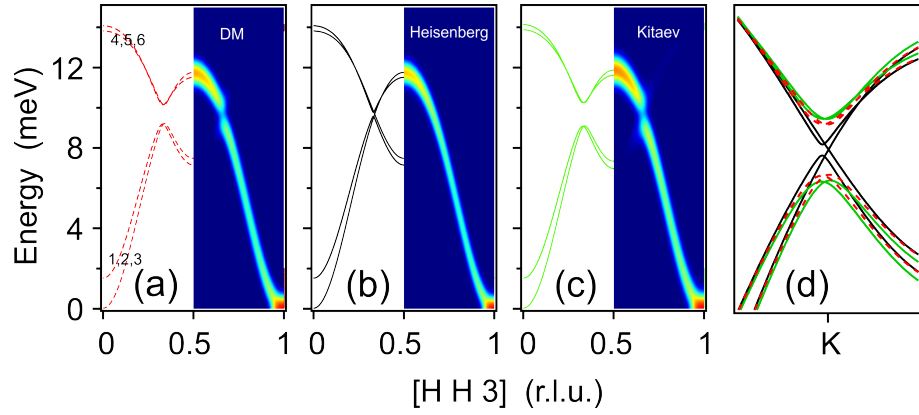


FIG. S8. **Comparison of the calculated magnon spectra with different models.** (a) Magnon spectra calculated by using the Heisenberg with 2nd-NN DM interaction model. Dash lines are the calculated magnon spectra at the BZ boundaries, and the intensity maps are the convoluted results with energy resolution of 1 meV. (b) Magnon spectra calculated by using a simple Heisenberg model. (c) Magnon spectra calculated by using the Heisenberg with a modified Kitaev interaction model. (d) Comparison of the magnon band dispersion near the Dirac point between all the models in (a-c).

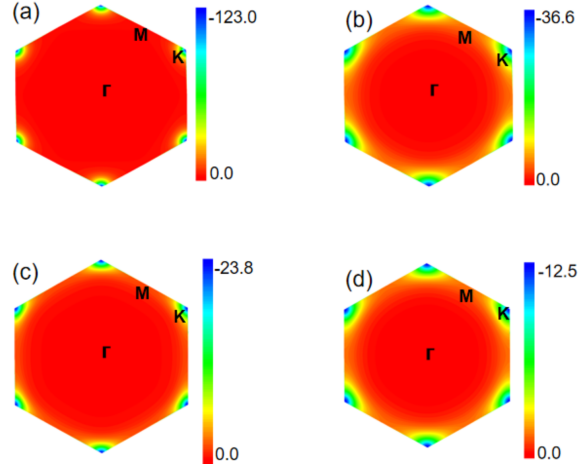


FIG. S9. **The calculated Berry curvature in the $K_x - K_y$ plane.** The Berry curvature for the lowest three magnon branches of bulk CrSiTe_3 (a) and CrGeTe_3 (b). The Berry curvature for the lowest branch of monolayer CrSiTe_3 (c) and CrGeTe_3 (d) in the first Brillouin zone. The Chern number is -3 for (a,b) and -1 for (c,d).

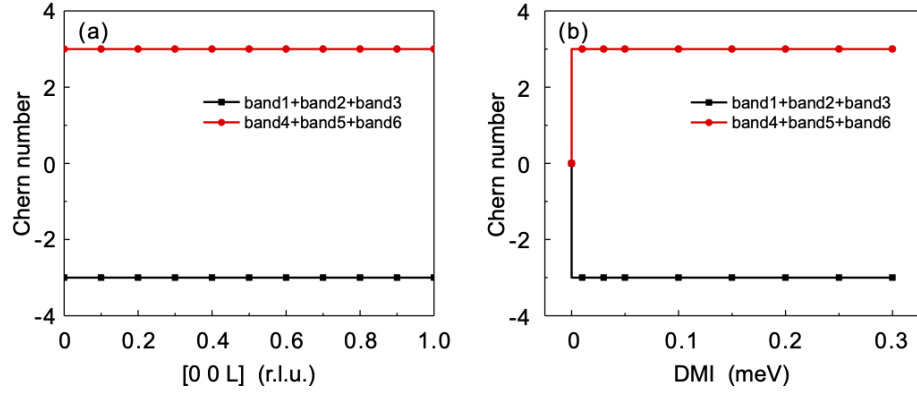


FIG. S10. **Chern numbers of magnon bands.** (a) The Chern number along the [0,0,L] direction. The sum of the Chern numbers are -3 and 3 for the lowest and highest three bands respectively. (b) The influence of the magnitude of the DM interaction on the Chern numbers of the bands.

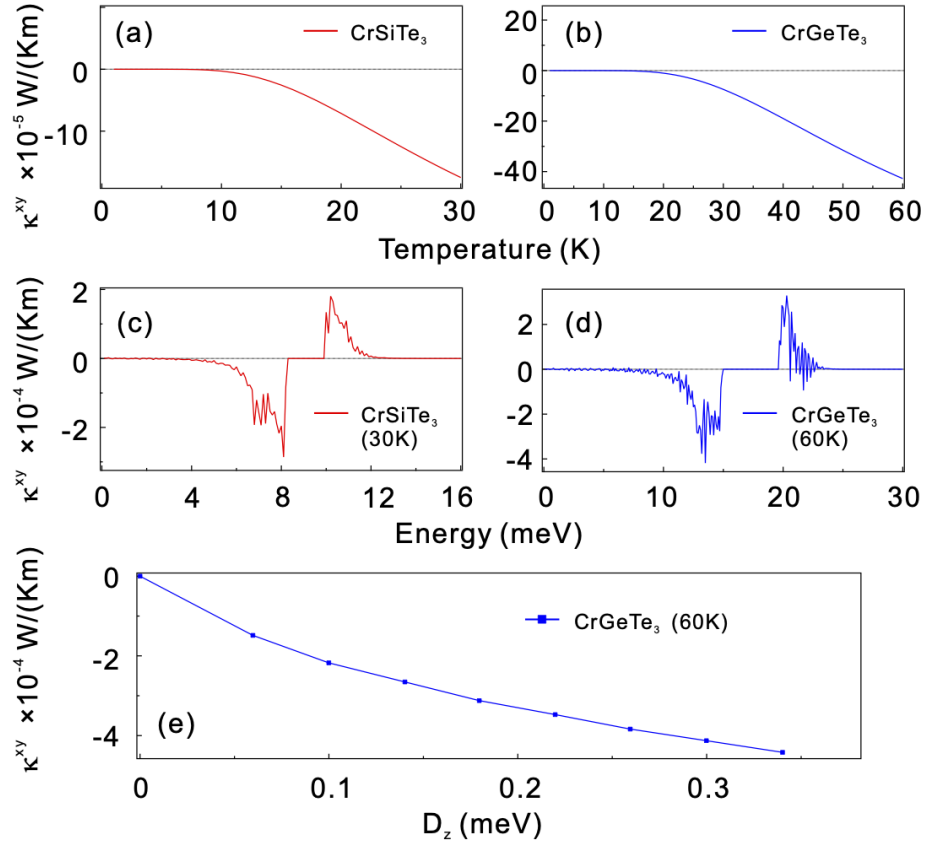


FIG. S11. **The calculated transverse thermal Hall conductivity (κ^{xy}) of CrGeTe₃ and CrSiTe₃.** The temperature dependence (a, b) and energy dependence (c, d) of the thermal Hall conductivity of CrGeTe₃ and CrSiTe₃. The κ^{xy} with the function of D_z for CrGeTe₃ at 60K is shown in (e).